VYSOKÁ ŠKOLA BÁŇSKÁ - TECHNICKÁ UNIVERZITA OSTRAVA
UNIVERZITNÍ STUDIJNÍ PROGRAMY

Bachelor thesis

Mueller matrix ellipsometry of special samples

Elipsometrie Muellerovy matice speciálních vzorků

Author: Přemysl Ciompa
Bachelor thesis superviser: doc. Dr. Mgr. Kamil Postava

Ostrava 2016

VŠB - Technical University of Ostrava
University Study Programmes
Katedra fyziky

Bachelor Thesis Assignment

Student:	**Přemysl Ciompa**
Study Programme:	B3942 Nanotechnology
Study Branch:	3942R001 Nanotechnology
Title:	Mueller matrix ellipsometry of special samples Elipsometrie Muellerovy matice speciálních vzorků
The thesis language:	English

Description:

The subject of the bachelor thesis is the Mueller matrix spectroscopic ellipsometry used for characterization of special samples. It includes experimental verification using the ellipsometer RC2 Woollam and consequent processing of experimental data.
The aim of the bachelor thesis belongs to the following areas:
- understanding special techniques of spectroscopic ellipsometry (measurement of thin film by a reflection through the substrate, measurement of anisotropic samples, measurement of weakly reflecting samples)
- spectroscopic ellipsometry of Sn films on a glass substrate, determination of their optical functions
- Mueller matrix ellipsometry of nonlinear BBO crystals (beta barium borate).

References:

1. E. Garcia-Caurel, et al., Advanced Mueller ellipsometry instrumentation and data analysis. Ellipsometry at the Nanoscale, Springer Berlin Heidelberg, 2013.
2. H. Fujiwara, Spectroscopic Ellipsometry: Principles and Applications, John Willey & Sons 2007.
3. R. M. A. Azzam and N. M. Bashara, Ellipsometry and Polarized Light, North-Holland, Amsterdam, 1977.
4. I. Ohlídal and D. Franta, in Progress in Optics, edited by E. Wolf North-Holland, Amsterdam, 2000, Vol. 41.

Extent and terms of a thesis are specified in directions for its elaboration that are opened to the public on the web sites of the faculty.

Supervisor: **doc. Dr. Mgr. Kamil Postava**

Consultant: Ing. Zuzana Mrázková

Date of issue: 20.10.2015

Date of submission: 16.05.2016

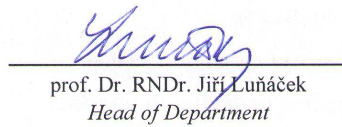

prof. Dr. RNDr. Jiří Luňáček
Head of Department

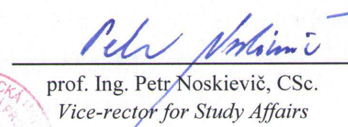

prof. Ing. Petr Noskievič, CSc.
Vice-rector for Study Affairs

Prohlašuji, že jsem tuto bakalářskou práci vypracoval samostatně s použitím odborné literatury a dalších informačních zdrojů, které jsou citovány na konci práce.

V Havířově dne 16. 05. 2016 ....

podpis autora

Prohlašuji, že,

- jsem byl seznámen s tím, že se na mou diplomovou práci plně vztahuje zákon č.121/2000 Sb., autorský zákon, zejména §35 - užití díla v rámci občanských a náboženských obřadů, v rámci školních představení a užití díla školního a §60 - školní dílo.

- beru na vědomí, že Vysoká škola báňská - Technická univerzita Ostrava (dále jen VŠB - TUO) má právo nevýdělečně ke své vnitřní potřebě diplomovou práci užít (§35 odst. 3).

- souhlasím s tím, že diplomová práce bude v elektronické podobě uložena v Ústřední knihovně VŠB - TUO k nahlédnutí a jeden výtisk bude uložen u vedoucího diplomové práce. Souhlasím s tím, že údaje o diplomové práci budou zveřejněny v informačním systému VŠB-TUO.

- bylo sjednáno, že s VŠB - TUO, v případě zájmu z její strany, uzavřu licenční smlouvu s oprávněním užít dílo v rozsahu §12 odst. 4 autorského zákona.

- bylo sjednáno, že užít své dílo - diplomovou práci nebo poskytnout licenci k jejímu využití mohu jen se souhlasem VŠB - TUO, která je oprávněna v takovém případě ode mne požadovat přiměřený příspěvek na úhradu nákladů, které byly VŠB - TUO na vytvoření díla vynaloženy (až do jejich skutečné výše).

- beru na vědomí, že odevzdáním své práce souhlasím se zveřejněním své práce podle zákona č.111/1988 Sb., o vysokých školách a o změně a doplnění dalších zákonů (zákon o vysokých školách), ve znění pozdějších předpisů, bez ohledu na výsledek její obhajoby.

V Havířově dne 16. 05. 2016 ....

jméno a příjmení studenta

adresa trvalého bydliště:

Hornická 659/22, Prostřední Suchá, 735 64 Havířov

I would like to thank doc. Dr. Mgr. Kamil Postava and Ing. Zuzana Mrázková for their help and guidance with writing this thesis.

Abstrakt

Tato bakalářská práce se zabývá použitím Elipsometrie Muellerových matic k charakterizaci speciálních vzorků. To zahrnuje měření na elipsometru RC2 Woollam a následné zpracování naměřených dat v softwaru CompleteEase. V této práci jsou zkoumány 3 typy vzorků a to systém tenkých vrstev Au/Cr na skleněném substrátu, vzorky Sn vrstev o tlouštkách 10, 20, 50 a 110 nm na skleněném substrátu a anizotropický BBO krystal. K charakterizaci vzorků bylo potřeba zvládnutí speciálních technik Elipsometrie Muellerových matic, jako je měření odrazem skrze substrát, analýza simultánním fitem dat z několika různých měření a měření a modelování anizotropických vzorků. Výsledkem práce je vytvoření optických modelů popisujících chování vzorků a popis dielektrických funkcí Au a Sn.

Klíčová slova: elipsometrie, elipsometrie Muellerových matic, BBO, Sn vrstvy, Au vrstvy, odraz skrze substrát, CompleteEase, beta baryum borate, tenké vrstvy

Abstract

The bachelor thesis deals with use of Mueller matrix Ellipsometry for characterization of special samples. It involves experimental measurement using RC2 Woollam ellipsometer and subsequental data analysis using CompleteEase software. Three types of samples are analyzed in this thesis, Au/Cr multilayer on a glass substrate, Sn thing layers 10, 20, 50 and 110 nm thick on a glass substrate and nonlinear BBO crystal. To characterize measured samples special techniques of Mueller matrix Ellipsometry had to be understood, like measurement using glass-side illumination, simultaneous fit of several different data sets and measurement and modeling of anisotropic samples. As a result of this thesis, the optical models characterizing samples‘ behaviour were constructed and the dielectric functions of Au and Sn were described.

Keywords: ellipsometry, Mueller matrix ellipsometry, BBO, Sn layers, Au layers, glass-side reflection, CompleteEase, beta baryum borate, thin layers

Contents

1. Introduction **12**

2. Theoretical background **14**

2.1 Reflection and transmission of light at planar interface 14
2.2 Jones calculus 15
2.3 Jones matrices of samples 16
2.4 Stokes vector 17
2.5 Mueller matrix 17
2.6 Mueller-Jones matrix 18
2.7 Anisotropic media 19
2.8 Yeh matrix method 21

3. Ellipsometric measurement and data analysis **24**

3.1 Mueller-matrix ellipsometry 24
3.2 General approach in data analysis 26
3.3 Dielectric function models 26
3.3.1 Tabulated data sets 26
3.3.2 Lorentz model 27
3.3.3 Sellmeier and Cauchy model 28
3.3.4 Drude model 28
3.3.5 B-spline model 28
3.3.6 Effective medium approximation 28
3.3.7 Kramers-Kronig relations 29
3.4 Depolarization effects 29

4. Au/Cr system on the glass substrate **34**

4.1 Substrate analysis 34
4.2 Au/Cr system analysis 36
4.3 Conclusion 39

5. Thin layers of Sn deposited on corning glass substrate **40**

5.1 Substrate analysis 40
5.2 Sn - 110 nm 42
5.3 Sn - 50 nm 45
5.4 Sn - 20 nm 47
5.5 Sn - 10 nm 48
5.6 Discussion 50

6. Anisotropic BBO crystal **51**

6.1 Optical axis aligned with z-axis 52
6.2 Optical axis aligned with y-axis 53
6.3 Optical axis aligned with x-axis 54
6.4 General alignment 55
6.5 Measurement 56

7. Conclusion **60**

8. References **62**

List of symbols and abbreviations

Vectors and matrices ... bold

Scalars .. italic

BBO .. Beta baryum borate

MSE .. Mean square error

$\langle\rangle$ .. temporal or spacial averaging

a^* .. complex conjugate

$\bigotimes$ .. Kronecker product

Ψ, Δ .. Ellipsomteric angles

EMA .. Effective medium approximation

ε .. the dielectric function

ψ, ϕ, θ .. Euler angles

1. Introduction

The ellipsometry has gone through rapid advancement in recent years with the development of new generation of Mueller matrix ellipsometers. It is now possible to measure all Mueller matrix elements in a matter of seconds. This fact allows the use of Mueller matrix ellipsometry for the real time ex and in situ measurements of whole variety of samples, depolarizing and anisotropic samples included. One of the most attractive applications of ellipsometry for industry is the real time monitoring of the thin film growth, [1] or even more complicated systems as nanoparticles [3] and nanotubes. [2]

Even though ellipsometry is a powerful analysis method, there are still limitations of its use. In cases when many parameters of the system are unknown the analysis can prove to be rather difficult and calculated data can be highly correlated. To overcome this problem, new approaches are being developed. One of these methods is an analysis using the glass side illumination, as has been shown in several published articles [4] [5] [6]. In this method the sample is illuminated through the substrate and even samples with high surface roughness or thick oxide layers can be analyzed.

In my thesis I discuss the theoretical background for data analysis of optical systems using Mueller matrix ellipsometry and then analyse several samples, Au/Cr/glass multilayer, oxidized Sn layer on glass substrate and anisotropic BBO crystal. The goal of measuring Au/Cr/glass sample is to precisely describe the system and to obtain the dielectric function of gold layer for further research. First, the glass substrate is modeled separately and then the data from regular reflection, glass side illumination and transmission are fitted simultaneously to obtain the best fit for the sample.

The second sample is oxidized Sn layer on the glass substrate. Sn has been recently researched as one of possible catalysts during silicon nanowires synthesis for new generation of solar cells. [7] During this process the metal catalyst is deposited on the substrate. Upon heating the small metal droplets are formed from the metal layer. In the next step the vapour precursors are introduced and it leads to incorporation of precursor inside the catalyst. Precursor then

precipitates at the surface-catalyst interface and Si nanowires are grown. For the proper optimization of Si nanowires the distribution and the density of metal droplets becomes important. If we would understand the optical properties of Sn thin films and metal droplets, ellipsometry could be used for an in situ analysis of growing Sn. This sample is also modeled by simultaneous fit of the data from the regular reflection and glass side illumination, however its data analysis is more complicated due to the high surface roughness and an oxide layer of unknown thickness.

The last sample to be analyzed in this thesis is an anisotropic BBO crystal widely used in non-linear optics. The goal is to understand the data analysis of anisotropic samples and to model its behaviour.

In the first section the basic physics of polarized light and propagation of light in anisotropic media are described. Second section describes Mueller matrix ellipsometry, general approach and dielectric function models used in data analysis. Depolarization effects, as they are significant while measuring data through a thick substrate, are also described. In the third, fourth and fifth section the data analysis of measured samples is performed.

2. Theoretical background

2.1 Reflection and transmission of light at planar interface

Because ellipsometry measures change in polarization upon reflection from sample, it is important to briefly discuss reflection and transmission of light. When light reaches interface between two mediums of different refractive indexes, part of light is refracted and continues to propagate and part of it is reflected. Refraction angle depends on well know Snell's law

$$n_i \sin\theta_i = n_t \sin\theta_t, \tag{2.1}$$

Figure 2.1: Reflection and refraction on a planar interface [10]

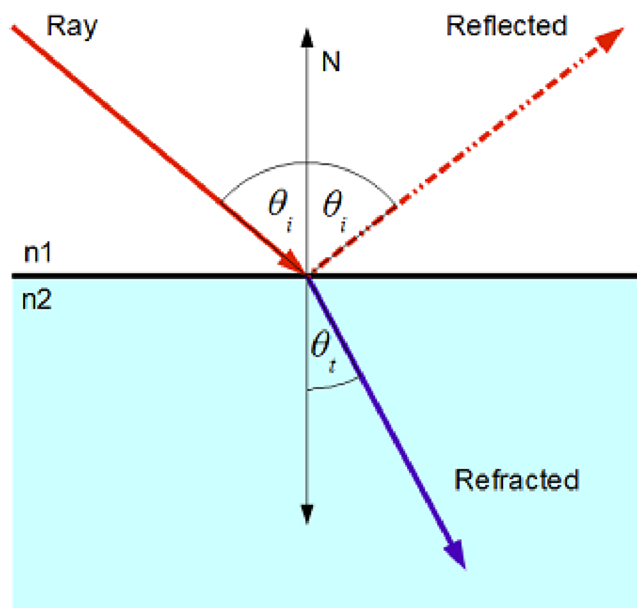

To describe reflection and transmission quantitatively, reflection and transmission co-

effiecients are defined.

$$r_p = \frac{E_{rp}}{E_{ip}} = \frac{n_t \cos\theta_i - n_i \cos\theta_t}{n_t \cos\theta_i + n_i \cos\theta_t}, \tag{2.2}$$

$$t_p = \frac{E_{tp}}{E_{ip}} = \frac{2n_i \cos\theta_i}{n_t \cos\theta_i + n_i \cos\theta_t}, \tag{2.3}$$

$$r_s = \frac{E_{rs}}{E_{is}} = \frac{n_i \cos\theta_i - n_t \cos\theta_t}{n_t \cos\theta_i + n_t \cos\theta_t}, \tag{2.4}$$

$$t_s = \frac{E_{ts}}{E_{is}} = \frac{2n_i \cos\theta_i}{n_i \cos\theta_i + n_t \cos\theta_t}, \tag{2.5}$$

These relations are derived using boundary conditions of Maxwell equations, which requires that tangential components of $\boldsymbol{E}$ and $\boldsymbol{H}$ are continuous at the interface. As we can see, p- (in the plane of incidence) and s-polarizations (perpendicular to the plane of incidence) behave differently. Reflection and transmission are in general complex numbers

$$r_p = |r_p| exp(i\delta_{rp}) \quad r_s = |r_s| exp(i\delta_{rs}) \tag{2.6}$$

$$t_p = |t_p| exp(i\delta_{tp}) \quad t_s = |t_s| exp(i\delta_{ts}) \tag{2.7}$$

From these equations we can interpret change of light upon reflection as change in amplitude nad change in phase of reflected light. This distinction is crucial for ellipsometric measurements.

However, in reality we are only able to measure intensities, so reflectance and transmitance must be defined.

$$R_p = \frac{I_{rp}}{I_{ip}} = |r_p|^2 \tag{2.8}$$

$$R_s = \frac{I_{rs}}{I_{is}} = |r_s|^2 \tag{2.9}$$

In the case of transmitance cross-sections also needs to be considered.

$$T_p = \frac{\Re(n_t \cos\theta_t)}{\Re(n_i \cos\theta_i)} |t_p|^2 \tag{2.10}$$

$$T_s = \frac{\Re(n_t \cos\theta_t)}{\Re(n_i \cos\theta_i)} |t_s|^2 \tag{2.11}$$

2.2 Jones calculus

Polarization of light can be understood as superposition of two waves oscillating in perpedicular directions. The Jones vector and Jones matrixes are usefull way of describing this phenomenon. Supposing we have the monochromatic plane wave travelling in z-direction oscillating along x and y axis. We can describe this state of polarization as

$$J = \begin{bmatrix} E_x \\ E_y \end{bmatrix} = \begin{bmatrix} E_{x0}\ exp(i\delta_x) \\ E_{y0}\ exp(i\delta_y) \end{bmatrix} \tag{2.12}$$

It is important to note that only fully polarized light can be described using the Jones vectors. To calculate the intensity of light, we have to multiply the Jones vector with its Hermitian adjoint

$$I \sim \boldsymbol{J}^{\dagger}\boldsymbol{J} \quad = \quad E_x E_x^* + E_y E_y^* \tag{2.13}$$

Upon interaction with the sample, light undergoes linear transformation. This interactions can be easily described using Jones matrixes.

$$E_x` = J_{11}E_x + J_{12}E_y \quad E_y` = J_{21}E_x + J_{22}E_y \tag{2.14}$$

$$\begin{bmatrix} E_x` \\ E_y` \end{bmatrix} = \begin{bmatrix} J_{11} & J_{12} \\ J_{21} & J_{22} \end{bmatrix} \begin{bmatrix} E_x \\ E_y \end{bmatrix} \tag{2.15}$$

For example linear a polarizer along x axis can be described as

$$J = \begin{bmatrix} 1 & 0 \\ 0 & 0 \end{bmatrix}$$

When dealing with multiple transformation, the total transformation is obtained by

$$J = J_n J_{n-1} ... J_2 J_1 \tag{2.16}$$

2.3 Jones matrices of samples

In general, the Jones matrix corresponding to transformation by reflection off the sample is described by

$$\begin{bmatrix} E_{rp} \\ E_{rs} \end{bmatrix} = \begin{bmatrix} r_{pp} & r_{ps} \\ r_{sp} & r_{ps} \end{bmatrix} \begin{bmatrix} E_{ip} \\ E_{is} \end{bmatrix} \tag{2.17}$$

For isotropic sample the matrix simplifies to

$$\begin{bmatrix} E_{rp} \\ E_{rs} \end{bmatrix} = \begin{bmatrix} r_p & 0 \\ 0 & r_p \end{bmatrix} \begin{bmatrix} E_{ip} \\ E_{is} \end{bmatrix} \tag{2.18}$$

For example, if we assume incident light $E_{ip} = E_{is} = 1$, reflected light will be transformed into

$$\begin{bmatrix} E_{rp} \\ E_{rs} \end{bmatrix} = \begin{bmatrix} r_p & 0 \\ 0 & r_p \end{bmatrix} \begin{bmatrix} E_{ip} \\ E_{is} \end{bmatrix} = \begin{bmatrix} r_p \\ r_s \end{bmatrix} \tag{2.19}$$

Matrix parameters can be calculated using thin layer optical models and then we can model behavior of the sample.

2.4 Stokes vector

Jones vectors are useful tool for describing totally polarized light but they can not describe unpolarized or partially polarized light. To handle such states, the Stokes vector needs to be used. Stokes vector has four parameters and deals with intensities.

$$\begin{aligned} S_0 &= I_x + I_y = \langle E_x E_x^* + E_y E_y^* \rangle, & (2.20)\\ S_1 &= I_x - I_y = \langle E_x E_x^* - E_y E_y^* \rangle, & (2.21)\\ S_2 &= I_{+45^\circ} - I_{-45^\circ} = \langle E_x E_y^* + E_y E_x^* \rangle, & (2.22)\\ S_3 &= I_R - I_L = i\langle E_x E_y^* + E_y E_x^* \rangle, & (2.23)\end{aligned}$$

where I_x, I_y, I_{+45° and I_{-45° represents intensities of polarization in x, y, +45° and -45° direction. I_R and I_L represents intensities of right- and left-circular polarization states. For totally polarized light the following equation must be satisfied

$$S_0^2 = S_1^2 + S_2^2 + S_3^2 \tag{2.24}$$

and for partially polarized light holds

$$S_0^2 > S_1^2 + S_2^2 + S_3^2 \tag{2.25}$$

It is convinient to describe degree of polarizazion as

$$p = \frac{\sqrt{S_1^2 + S_2^2 + S_3^2}}{S_0}, \tag{2.26}$$

Therefore, for totally polarized light $p = 1$ and for unpolarized light $p = 0$. Stokes vector and its corresponding state of polarization can be also represented visually with the Poincaré sphere.

Last three parameteres of Stokes vector represent a point on the surface of the sphere, in the case of totally polarized light, or point inside of the sphere in the case of partially polarized light. Unpolarized light is described by the origin. Points on the equator of the sphere represent linear polarization states, points on the north hemisphere are left-elliptical states, on the south hemispehere right-elliptical states and points on the poles represent corresponding circular polarization states. The radius of the sphere can be normalized or defined as $r = S_0$.

2.5 Mueller matrix

Similarly as Jones matrices describe transformation of Jones vectors, Mueller matrices are used to describe transformation of Stokes vectors. This 4×4 matrix is able to describes not only

Figure 2.2: Poincaré sphere [11]

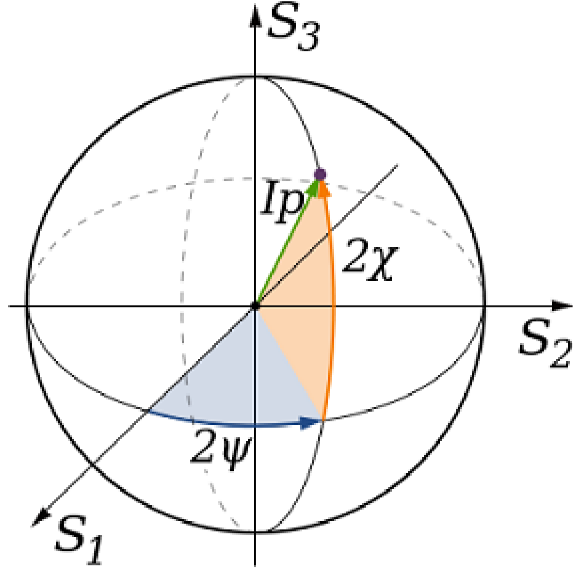

transformation of fully polarized light, but can also describe depolarization effects of the sample.

$$\begin{bmatrix} S_0' \\ S_1' \\ S_2' \\ S_3' \end{bmatrix} = M \begin{bmatrix} S_0 \\ S_1 \\ S_2 \\ S_3 \end{bmatrix} = \begin{bmatrix} M_{00} & M_{01} & M_{02} & M_{03} \\ M_{10} & M_{11} & M_{12} & M_{13} \\ M_{20} & M_{21} & M_{22} & M_{23} \\ M_{30} & M_{31} & M_{32} & M_{33} \end{bmatrix} \begin{bmatrix} S_0 \\ S_1 \\ S_2 \\ S_3 \end{bmatrix}. \tag{2.27}$$

2.6 Mueller-Jones matrix

In the case of non-depolarizing samples we can calculate the Mueller matrix from sample‘s Jones matrix. Because Mueller calculus deals with intensities, we need to find transformations of the interactions using Jones matrix components. From (2.40) we get

$$(E_i E_j^*)^{out} = \sum_{k,l} J_{ik} J_{jl}^* (E_k E_l^*)^{in}, \tag{2.28}$$

For linear non-depolarizing sample we can write this equation as

$$C^{out} = F C^{in}, \tag{2.29}$$

where

$$C = \begin{bmatrix} \langle E_p E_p^* \rangle \\ \langle E_p E_s^* \rangle \\ \langle E_s E_p^* \rangle \\ \langle E_s E_s^* \rangle \end{bmatrix} \qquad F = J \otimes J^* = \begin{bmatrix} \langle J_{pp} J_{pp}^* \rangle & \langle J_{pp} J_{ps}^* \rangle & \langle J_{ps} J_{pp}^* \rangle & \langle J_{ps} J_{ps}^* \rangle \\ \langle J_{pp} J_{sp}^* \rangle & \langle J_{pp} J_{ss}^* \rangle & \langle J_{ps} J_{sp}^* \rangle & \langle J_{ps} J_{ss}^* \rangle \\ \langle J_{sp} J_{pp}^* \rangle & \langle J_{sp} J_{ps}^* \rangle & \langle J_{ss} J_{pp}^* \rangle & \langle J_{ss} J_{ps}^* \rangle \\ \langle J_{sp} J_{sp}^* \rangle & \langle J_{sp} J_{ss}^* \rangle & \langle J_{ss} J_{sp}^* \rangle & \langle J_{ss} J_{ss}^* \rangle \end{bmatrix}. \tag{2.30}$$

C represents the coherency vector. This vector also fully describes any polarization state as it containts second moments of electric field distributions. This vector can be easily transformed to Stokes vector (x-axis aligned with p- and y-axis with s-)

$$S = \begin{bmatrix} \langle E_p E_p^* + E_s E_s^* \rangle \\ \langle E_p E_p^* - E_s E_s^* \rangle \\ \langle E_p E_s^* + E_s E_p^* \rangle \\ i\langle E_p E_s^* - E_s E_p^* \rangle \end{bmatrix} = AC, \tag{2.31}$$

where

$$A = \begin{bmatrix} 1 & 0 & 0 & 1 \\ 1 & 0 & 0 & -1 \\ 0 & 1 & 1 & 0 \\ 0 & i & -i & 0 \end{bmatrix}. \tag{2.32}$$

From these equations we obtain that

$$M = AFA^{-1} = A(J \otimes J^*)A^{-1}. \tag{2.33}$$

For isotropic nondepolarizing samples the Mueller matrix becomes

$$M \approx \begin{bmatrix} 1 & -N & 0 & 0 \\ -N & 1 & 0 & 0 \\ 0 & 0 & C & S \\ 0 & 0 & -S & C \end{bmatrix} \tag{2.34}$$

where

$$N = \cos 2\Psi \tag{2.35}$$

$$S = \sin 2\Psi \sin\Delta \tag{2.36}$$

$$C = \sin 2\Psi \cos\Delta \tag{2.37}$$

$$\tan\Psi \exp(i\Delta) = \frac{C + iS}{1 + N} \tag{2.38}$$

2.7 Anisotropic media

In the case of the isotropic medium, the electromagnetic wave can be divided into two arbitrary independent orthogonal eigenmodes, which propagate through the medium without any change. However, this is no longer truth for an anisotropic medium where exists only two

independent eigenmodes. Furthermore, the dielectric constant is different for both eigenmodes. The wave equation for the anisotropic medium is

$$k_0^2\hat{\varepsilon}\boldsymbol{E_0} - \boldsymbol{k}^2.\boldsymbol{E_0} + \boldsymbol{k}.(\boldsymbol{k}\boldsymbol{E_0}) = 0 \tag{2.39}$$

where

$$\boldsymbol{k} = k_x\boldsymbol{x} + k_y\boldsymbol{y} + k_z\boldsymbol{z} = k_0\left(N_x\boldsymbol{x} + N_y\boldsymbol{y} + N_z\boldsymbol{z}\right). \tag{2.40}$$

Let‘s assume an isotropic/anisotropic interface with coordinate system, such that N_z is orthogonal to the interface and $N_x = 0$. The anisotropic medium is then described by the dielectric tensor $\hat{\varepsilon}$

$$\hat{\varepsilon} = \begin{pmatrix} \varepsilon_{11} & \varepsilon_{12} & \varepsilon_{13} \\ \varepsilon_{21} & \varepsilon_{22} & \varepsilon_{23} \\ \varepsilon_{31} & \varepsilon_{32} & \varepsilon_{33} \end{pmatrix} \tag{2.41}$$

and by substituting into (2.41) we get

$$\begin{pmatrix} \varepsilon_{11} - N_y^2 - N_z^2 & \varepsilon_{12} & \varepsilon_{13} \\ \varepsilon_{21} & \varepsilon_{22} - N_z^2 & \varepsilon_{23} + N_yN_z \\ \varepsilon_{31} & \varepsilon_{32} + N_yN_z & \varepsilon_{33} - N_y^2 \end{pmatrix} \begin{bmatrix} E_{0x} \\ E_{0y} \\ E_{0z} \end{bmatrix} = 0, \tag{2.42}$$

where

$$N_y = \sin\alpha.n \tag{2.43}$$

α is the incidence angle and n is the index refraction of the isotropic medium. This equation has non-trivial solutions only if $\det() = 0$, so by solving

$$\begin{aligned} \varepsilon_{33}N_z^4 + (\varepsilon_{23} + \varepsilon_{32}N_yN_z^3 - [\varepsilon_{22}(\varepsilon_{33} - N_y^2) + \varepsilon_{33}(\varepsilon_{11} + N_y^2) - \varepsilon_{13}\varepsilon_{31} - \varepsilon_{23}\varepsilon_{32}]N_z^2 \\ -[(\varepsilon_{11} - N_y^2)(\varepsilon_{23} + \varepsilon_{32}) - \varepsilon_{12}\varepsilon_{31} - \varepsilon_{23}\varepsilon_{13}]N_yN_z + \varepsilon_{22}[(\varepsilon_{11} - N_y^2)(\varepsilon_{33} - N_y^2) - \varepsilon_{12}\varepsilon_{21}] \\ -\varepsilon_{12}\varepsilon_{21}(\varepsilon_{33} - N_y^2) - \varepsilon_{23}\varepsilon_{32}(\varepsilon_{11} - N_y^2) + \varepsilon_{12}\varepsilon_{31}\varepsilon_{23} + \varepsilon_{21}\varepsilon_{13}\varepsilon_{32} = 0 \end{aligned} \tag{2.44}$$

we get 4 N_{zi} corresponding to 4 propagating waves in the anisotropic medium. Their polarizations are

$$\boldsymbol{e_i} = C\begin{pmatrix} -\varepsilon_{12}(\varepsilon_{33} - N_y^2) + \varepsilon_{13}(\varepsilon_{32} + N_yN_{zi}) \\ (\varepsilon_{33} - N_y^2)(\varepsilon_{11} - N_y^2 - N_{zi}^2) - \varepsilon_{13}\varepsilon_{31} \\ -(\varepsilon 11 - N_y^2 - N_{zi}^2)(\varepsilon_{32} + N_yN_{zi}) + \varepsilon_{31}\varepsilon 12 \end{pmatrix} \tag{2.45}$$

$$\boldsymbol{b_i} = (N_y\boldsymbol{y} + N_{zi}\boldsymbol{z}) \times \boldsymbol{e_i} \tag{2.46}$$

where C is normalization constant such that $\boldsymbol{e_i}.\boldsymbol{e_i} = 1$. It is important to note, that this expression cannot be used in cases with higher symmetry, when

$$(\varepsilon_{11} - N_y^2 - N_{zi}^2) = 0. \tag{2.47}$$

This can be a problem escpecially during computer calculations and such cases must be handled separately.

2.8 Yeh matrix method

Propagation of monochromatic plane wave in anisotropic layered media can be described by 4×4 matrix algebra. The boundary conditions require that

$$E_x^{(n-1)} = E_x^{(n)}, E_y^{(n-1)} = E_y^{(n)} \tag{2.48}$$

$$H_x^{(n-1)} = H_x^{(n)}, H_y^{(n-1)} = H_y^{(n)} \tag{2.49}$$

is satisfied everywhere in the medium. The electric field in nth layer can be written as

$$\boldsymbol{E} = \sum_{i=1}^{4} E_0 \boldsymbol{e_i} \exp\{i[\omega t - k_0(N_y y + N_{zi} z)]\}, \tag{2.50}$$

thus the electric field at the (n-1)/n interface and the electric field at the n/(n+1) interface are related in the following way.

$$\begin{pmatrix} e_{x1}^{(n-1)} & e_{x2}^{(n-1)} & e_{x3}^{(n-1)} & e_{x4}^{(n-1)} \\ b_{y1}^{(n-1)} & b_{y2}^{(n-1)} & b_{y3}^{(n-1)} & b_{y4}^{(n-1)} \\ e_{y1}^{(n-1)} & e_{y2}^{(n-1)} & e_{y3}^{(n-1)} & e_{y4}^{(n-1)} \\ b_{x1}^{(n-1)} & b_{x2}^{(n-1)} & b_{x3}^{(n-1)} & b_{x4}^{(n-1)} \end{pmatrix} \begin{pmatrix} E_1^{(n-1)} \\ E_2^{(n-1)} \\ E_3^{(n-1)} \\ E_4^{(n-1)} \end{pmatrix} = \begin{pmatrix} e_{x1}^{(n)} & e_{x2}^{(n)} & e_{x3}^{(n)} & e_{x4}^{(n)} \\ b_{y1}^{(n)} & b_{y2}^{(n)} & b_{y3}^{(n)} & b_{y4}^{(n)} \\ e_{y1}^{(n)} & e_{y2}^{(n)} & e_{y3}^{(n)} & e_{y4}^{(n)} \\ b_{x1}^{(n)} & b_{x2}^{(n)} & b_{x3}^{(n)} & b_{x4}^{(n)} \end{pmatrix} \times$$
$$\begin{pmatrix} \exp(ik_0 N_{z1}^{(n)} d^{(n)}) & 0 & 0 & 0 \\ 0 & \exp(ik_0 N_{z2}^{(n)} d^{(n)}) & 0 & 0 \\ 0 & 0 & \exp(ik_0 N_{z3}^{(n)} d^{(n)}) & 0 \\ 0 & 0 & 0 & \exp(ik_0 N_{z4}^{(n)} d^{(n)}) \end{pmatrix} \begin{pmatrix} E_1^{(n)} \\ E_2^{(n)} \\ E_3^{(n)} \\ E_4^{(n)} \end{pmatrix} \tag{2.51}$$

This equation can be written as

$$D^{(n-1)} E_0^{(n-1)} = D^{(n)} P^{(n)} E_0^{(n)}, \tag{2.52}$$

where $\mathbf{D^n}$ is the Dynamic matrix of nth layer and $\mathbf{P^n}$ is propagation matrix of nth layer.

$$D^{(n)} = \begin{pmatrix} e_{x1}^{(n)} & e_{x2}^{(n)} & e_{x3}^{(n)} & e_{x4}^{(n)} \\ b_{y1}^{(n)} & b_{y2}^{(n)} & b_{y3}^{(n)} & b_{y4}^{(n)} \\ e_{y1}^{(n)} & e_{y2}^{(n)} & e_{y3}^{(n)} & e_{y4}^{(n)} \\ b_{x1}^{(n)} & b_{x2}^{(n)} & b_{x3}^{(n)} & b_{x4}^{(n)} \end{pmatrix} \tag{2.53}$$

$$P^{(n)} = \begin{pmatrix} \exp(ik_0 N_{z1}^{(n)} d^{(n)}) & 0 & 0 & 0 \\ 0 & \exp(ik_0 N_{z2}^{(n)} d^{(n)}) & 0 & 0 \\ 0 & 0 & \exp(ik_0 N_{z3}^{(n)} d^{(n)}) & 0 \\ 0 & 0 & 0 & \exp(ik_0 N_{z4}^{(n)} d^{(n)}) \end{pmatrix} \tag{2.54}$$

Let‘s assume we have only a simple interface between two media. Then $\mathbf{E_0}$ is during propagation transformed by

$$E_0^{(0)} = \left[D^{(0)}\right]^{-1} D^{(1)} E_0^{(1)} \tag{2.55}$$

$$E_0^{(0)} = M E_0^{(1)} \tag{2.56}$$

$$M = \left[D^{(0)}\right]^{-1} D^{(1)} \tag{2.57}$$

$$M = \begin{pmatrix} M_{11} & M_{12} & M_{13} & M_{14} \\ M_{21} & M_{22} & M_{23} & M_{24} \\ M_{31} & M_{32} & M_{33} & M_{34} \\ M_{31} & M_{32} & M_{33} & M_{34} \end{pmatrix} \tag{2.58}$$

where $\mathbf{M}$ is total matrix of the whole multilayer system. The same approach can be used for systems with more layers. From this matrix reflection and transmission coefficients can be calculated.

$$r_{ss} = \left.\frac{E_2^{(0)}}{E_1^{(0)}}\right|_{E_3^{(0)}=0} = \frac{M_{21}M_{33} - M_{23}M_{31}}{M_{11}M_{33} - M_{13}M_{31}} \tag{2.59}$$

$$r_{sp} = \left.\frac{E_4^{(0)}}{E_1^{(0)}}\right|_{E_3^{(0)}=0} = \frac{M_{41}M_{33} - M_{43}M_{31}}{M_{11}M_{33} - M_{13}M_{31}} \tag{2.60}$$

$$r_{ps} = \left.\frac{E_2^{(0)}}{E_3^{(0)}}\right|_{E_1^{(0)}=0} = -\frac{M_{11}M_{23} - M_{13}M_{21}}{M_{11}M_{33} - M_{13}M_{31}} \tag{2.61}$$

$$r_{pp} = \left.\frac{E_4^{(0)}}{E_3^{(0)}}\right|_{E_1^{(0)}=0} = -\frac{M_{11}M_{43} - M_{13}M_{41}}{M_{11}M_{33} - M_{13}M_{31}} \tag{2.62}$$

These coefficients can be now used to formulate the Jones matrix of the sample (2.17), from which the Mueller-Jones matrix can be calculated (2.33). Anisotropic Mueller-Jones matrix is no longer simple and requiers seven parameters to be fully described.

3. Ellipsometric measurement and data analysis

In ellipsometry, we irradiate sample with light waves and from the change of polarization state we calculate the optical constants or different parameters of the sample. Change of polarization originates from different behaviour of p- and s-polarizations upon reflection. In traditional ellipsometry the state of polarization is represented by two quantities, Ψ and Δ.

$$\rho = \tan\Psi \exp(i\Delta) = \frac{r_p}{r_s} \tag{3.1}$$

We can calculate Ψ and Δ from reflection coefficient as follows

$$\Psi = \tan^{-1}(|\rho|) = \tan^{-1}\sqrt{\frac{R_p}{R_s}} \tag{3.2}$$

$$\Delta = \arg(\rho). \tag{3.3}$$

However, nowadays more advanced ellipsometers are able to measure directly Mueller matrix elements of the sample.

3.1 Mueller-matrix ellipsometry

There are many types of ellipsometry instruments. Traditionally ellipsometry instruments measured Ψ and Δ parameters. However, this approach is not sufficient to characterize depolarizing and anisotropic samples. In such cases Mueller-matrix ellipsomtery needs to be applied. This technique allows direct measurement of Mueller matrix corresponding to the sample.

All ellipsometers consist of a light source, a polarization state generator (PSG) and a polarization state analyzer (PSA). Spectroscopic ellipsometers also use monochromator/spectrograph in their designs. Propagating light beam changes its state when going through PSG, upon reflection from the sample and then when it goes through PSA. The passing beam is modulated before or/and after the sample and elements of Mueller matrix are calculated from measured

intensity function. Generally, we can divide ellipsometers into two categories depending on how the polarization state is modulated. Modulation can be introduced by phase modulation by applying a mechanical stress, a magnetic or an electric field or by physically rotating optical elements in PSG or PSA.

Figure 3.1: Three different rotating-elements designs [12]

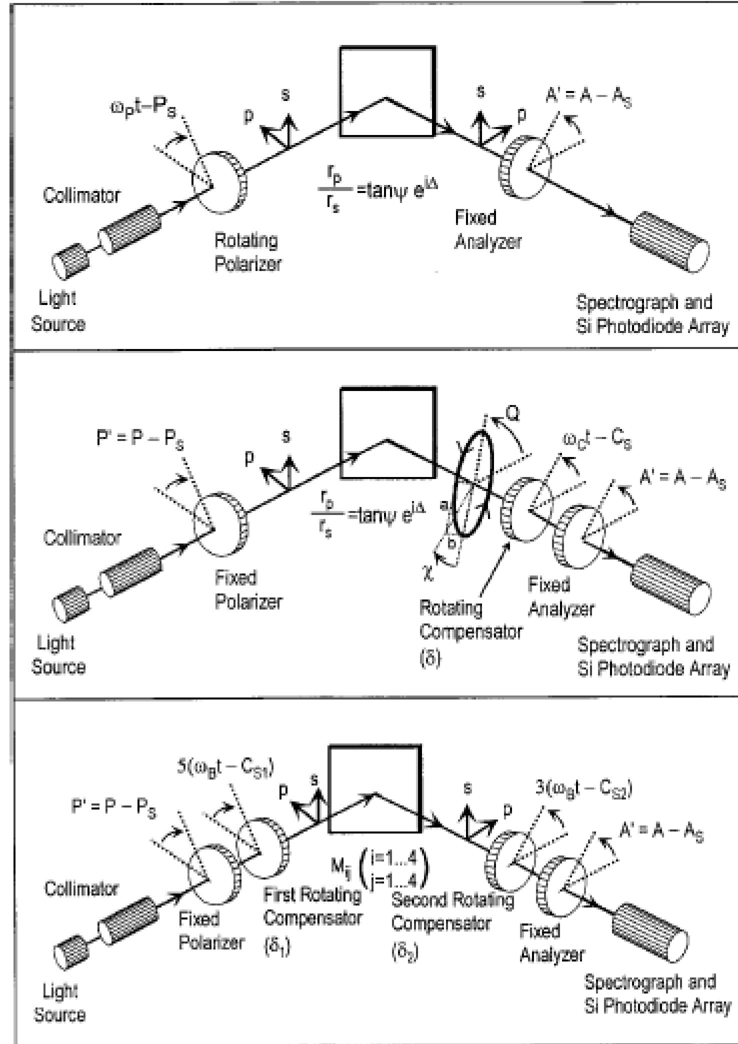

There are many different designs but two configurations have been widely generalized [12], due to their ability to access the full Mueller matrix and possibility of real time measurements, the double rotating-compensator and photoelastic modulator design. Rotating compensator configuration PC_RSC_RA consists of two compensators, one placed between polarizer and the sample at the entry arm and the other between the sample and analyzer at the exit arm. They rotate synchronously with each other at the specific frequency ratios, 5:l where l = 1, ...,4. This configuration allows to measure the full Mueller matrix in a single run. The ellipsometers based

on photoelastic modulators consists four modulators placed between the polarizer and the sample and between the sample and analyzer, which vibrate at different frequencies. The four modulator configuration also enables to measure the whole Mueller matrix in a single run.

3.2 General approach in data analysis

To analyze measured data accurately, the layered optical model, which corresponds to the sample structure, must be built. Each layer is characterized by its thickness and optical constants. Using created model ellipsometric data are generated and compared to measured data. The agreement between measured and generated data is then improved by fitting some of the model parameters and the results are evaluated. If the results are not acceptable, the model or its parameters must be modified until better fit is acquired.

Data analysis in this thesis is done by CompleteEase software. Using this software even more complex phenomena, such as surface rougness, graded layers, backside reflection, thickness inhomogenities etc. can be modeled.

To quantify " a goodness of fit" the MSE value is defined (definition according to the CompleteEase manual)

$$MSE = \sqrt{\frac{1}{3n-m}\sum_{i=1}^{n}\left[(N_{Ei}-N_{Gi})^2+(C_{Ei}-C_{Gi})^2+(S_{Ei}-S_{Gi})^2\right]} \times 1000, \tag{3.4}$$

where n is the number of measured wavelenghts, m is the number of fit parameters and N, C, S are components of a Mueller matrix.

The most crucial process of data analysis is evaluating the fit results. To deem a model acceptable, the following conditions must be met. The generated data must fit measured data, model should be unique and fitted parameters physical.

3.3 Dielectric function models

In order to model a sample‘s behaviour accurately, it is necessary to obtain realistic dielectric function of modeled layers from tabulated data sets or by using appropriate model.

3.3.1 Tabulated data sets

One approach is using tabulated data sets of used materials. This can be good starting point, however one has to be cautious as optical constants of thin films often vary from their bulk counterparts. Furthermore, thin films are often polycrystalline or amorphous and their

optical properties vary according to their fabrication conditions. Other effects that can possibly influence dielectric function are interfaces, which can cause different stress in the material, and interface layers. Even though many problems can arise while using tabulated data sets, they are still good starting point during data analysis.

3.3.2 Lorentz model

The Lorentz model is a classical model describing the solid as a collection of non-interacting oscillators. It assumes that negatively charged electron is bound to the postively charged nucleus by spring like force and oscillates in a viscous fluid. The incoming electric field induces polarization and electron starts to oscillate.

$$m_e \frac{d^2x}{dt^2} = -m_e \Gamma \frac{dx}{dt} - m_e \omega_0^2 x - eE_0 \exp(i\omega t) \tag{3.5}$$

The first term on the right side of the equation represents the damping force of the viscous fluid, where Γ represents damping coefficient. The second term represents the restoring force of the spring according to Hook‘s law ($F = -kx, \omega_0 = \sqrt{k/m}$ and the last term represents the electrostatic force. This equation describes forced oscillation of the electron at the same frequency as the applied electric field. Assuming the solution will be in the form of $x(t) = a\exp(i\omega t)$ and substituting it into the equation we get

$$a = -\frac{eE_0}{m_e} \frac{1}{(\omega_0^2 - \omega^2) + i\Gamma\omega} \tag{3.6}$$

The dielectric polarization is expressed as $P = ql = -eN_e x(t)$, where N_e is electron density. From these equations we can express dielectric constant as

$$\varepsilon = 1 + \frac{P}{\varepsilon_0 E} = 1 + \frac{eN_e a \exp(i\omega t)}{\varepsilon_0 E_0 \exp(i\omega t)} = \frac{e^2 N_e}{\varepsilon_0 m_e} \frac{1}{(\omega_0^2 - \omega^2) + i\Gamma\omega} \tag{3.7}$$

$$\varepsilon_1 = 1 + \frac{e^2 N_e}{\varepsilon_0 m_e} \frac{(\omega_0^2 - \omega^2)}{(\omega_0^2 - \omega^2)^2 + \Gamma^2\omega^2} \tag{3.8}$$

$$\varepsilon_2 = 1 + \frac{e^2 N_e}{\varepsilon_0 m_e} \frac{\Gamma\omega}{(\omega_0^2 - \omega^2)^2 + \Gamma^2\omega^2} \tag{3.9}$$

As we can see the dielectric constant is function of the light‘s frequency and depends on the resonant frequency of the particular material. Expressing the Lorentz oscillator as a function of energy, we get

$$\varepsilon(E) = \varepsilon(E) = 1 + \frac{A}{E_0^2 - E^2 + i\Gamma E} \tag{3.10}$$

The Lorentz model is not used directly during data analysis in this thesis, however other models derived from the Lorentz model are.

3.3.3 Sellmeier and Cauchy model

The Sellmeier model can be applied to model transparent regions and it is derived from the Lorentz model by assuming the dampening coefficient $\Gamma = 0$. We get commonly known expression

$$\varepsilon = \varepsilon_1 = A + \frac{B\lambda^2}{\lambda^2 - \lambda_0^2} \tag{3.11}$$

By further approximations we get Cauchy model for the refraction index

$$n = A + \frac{B}{\lambda^2} + \frac{C}{\lambda^4} ... \tag{3.12}$$

3.3.4 Drude model

The Drude model is used for describing free carrier effects in metals and semiconductors and is also derived from the Lorentz model, by assuming that electron is free and there is no force holding it to the nucleus. Therefore $\omega_0 = 0$ and we get

$$\varepsilon(E) = \varepsilon(E) = 1 - \frac{A}{E}\left(\frac{1}{E - i\Gamma}\right) \tag{3.13}$$

3.3.5 B-spline model

The CompleteEase softwares enables use of B-spline model [16] as alternative to both tabulated data sets as to oscillator models. The B-spline model interpolates the dielectric function by dividing spectral range into series of nodes. The dielectric function between nodes is then interpolated by the basic spline curve. The resulting curve is produced by adding weighted functions at each node. The B-spline model allows very flexible and continuous curves. Furthermore, it allows to assume transparent regions, different node spacing, tie-offs beyond the measured range and other options. It also allows use of Kramer-Kronig mode, when only ε_2 spectrum is interpolated and ε_1 is calculated.

3.3.6 Effective medium approximation

The multilayered optical systems often include interface layers such as surface rougness, inohomogenous oxide layeres etc. Such layers can be analyzed by applying effective medium theories. The effective medium (EMA) dielectric function is based on dielectric functions of two or more composite materials. There are free most common effective medium approximations,

which can be jointly expressed as

$$\frac{\langle\varepsilon\rangle - \varepsilon_h}{\langle\varepsilon\rangle + \gamma\varepsilon_h} = \sum_j f_j \frac{\varepsilon_j - \varepsilon_h}{\varepsilon_j + \gamma\varepsilon_h}, \tag{3.14}$$

where $\langle\varepsilon\rangle$ is the dielectric function of the effective medium, ε_h is the dielecric function of the host medium, ε_j is the dielectric function of the j-th consituent, f_j is a volume fraction of j-th constituent and γ is factor related to the shape of the inclusions. The different models then differ only by the choice of the host material. Lorentz-Lorentz assumes air as the host material and so $\varepsilon_h = 1$. The Maxwell-Garnett assumes that host material is the material with highest constituent fraction and the Bruggeman model assumes the host material is the effective layer itself, $\varepsilon_h = \langle\varepsilon\rangle$. During data analysis in this thesis the Bruggeman model was used.

3.3.7 Kramers-Kronig relations

The real and imaginary parts of the dielectric function are not independent, but must satisfy Kramer-Kronig relations.

$$\varepsilon_1(\omega) = 1 + \frac{2}{\pi} P \int_0^\infty \frac{\omega^{‘}\varepsilon_2(\omega^{‘})}{\omega^{‘2} - \omega^2} d\omega^{‘} \tag{3.15}$$

$$\varepsilon_2(\omega) = -\frac{2\omega}{\pi} P \int_0^\infty \frac{\varepsilon_1(\omega^{‘}) - 1}{\omega^{‘2} - \omega^2} d\omega^{‘} \tag{3.16}$$

The fact that physically correct models must satisfy Kramers-Kronig relations has to be taken into account while modeling dielectric functions of materials.

3.4 Depolarization effects

Even though the CompleteEase software can model depolarization effects, it is important to understand their causes and approaches used to include these phenomena in optical models. In cases when a sample depolarizes light, there is no direct relation between Jones and Mueller formalism and sample has to be described using Mueller matrices. Depolarization effect of the sample can be quantified using quadratic depolarization index

$$P_q = \sqrt{\frac{\sum_{ij} M_{ij}^2 - M_{11}^2}{3M_{11}^2}}. \tag{3.17}$$

There are several reasons for depolarization upon reflection:

- backside reflections
- thickness non-uniformity

- surface roughness
- incident angle variation
- wavelength variation

The depolarization by backside reflection is caused by the long optical pass length through the substrate. This unables us to define the phase of light at the interface, as it changes with time, and we need to regard this light as incoherent. Subsequent incoherent integration of the light coming from the backside and the one reflected from the surface results in partially polarized light entering the detector. This phenomenon can be amplified by thickness non-uniformity. The light from one part of light spot experiences different thickness than from the others and if incoherent condition holds, it undergoes different change of polarization. Reflected light is a superposition of different polarization states and this results in the quasi-depolarization upon integration by the detector. When surface roughness is high, multiple reflections can occur before light reaches detector and some amount of light is scattered and never reaches the detector. Multiple polarization states are also generated in this case. Incident angle variation has similiar effect, as it also generates different states, and it can be an issue especially when focusing probe is used. Depolarization originating from wavelength variation is introduced by monochromator. Monochromators are not perfectly monochromatic devices so different wavelengths are measured at the same time by the light detector.

Figure 3.2: Depolarization by backside reflection [13]

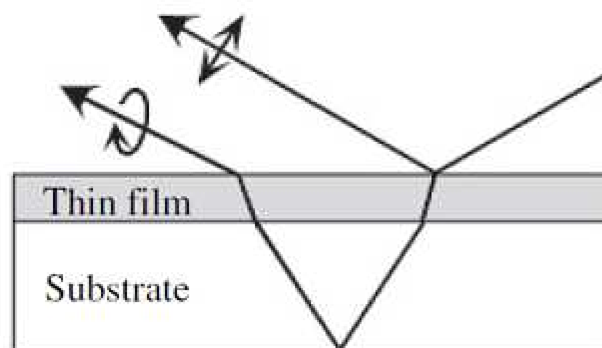

There are several methods that can eliminate unwanted depolarization effects. Backside reflection can be easily eliminated by roughening the back surface, coating it with black paint so light will be absorbed or using index-matching liquid to couple the substrate with similiar material and basically removing the interface. Thickness non-uniformity can be minimized by

focusing the light beam to lower spot size, but it can lead to higher incident angle variation. Huge surface roughness can be removed by polishing the sample, but it may lead to damaged interface layer which needs to be accounted for in our calculations. However, sometimes we cannot optimize sample structure. In such cases depolarization has to be included in our optical model.

In the case when sample acts as simple depolarizer, its Mueller matrix can be decomposed as

$$M = \beta M_J + (1-\beta)D = \beta M_J + (1-\beta)\begin{bmatrix} 1 & 0 & 0 & 0 \\ 0 & 0 & 0 & 0 \\ 0 & 0 & 0 & 0 \\ 0 & 0 & 0 & 0 \end{bmatrix}, \tag{3.18}$$

where M_J represents Mueller-Jones matrix and β is fraction of polarized light. In case of the isotropic sample the Mueller matrix is

$$M = \begin{bmatrix} 1 & -N_S & 0 & 0 \\ -N_S & \beta & 0 & 0 \\ 0 & 0 & C_S & S_S \\ 0 & 0 & -S_S & C_S \end{bmatrix}, \tag{3.19}$$

where

$$N_S = \beta N, C_S = \beta C, S_S = \beta S, \tag{3.20}$$

$$(N_S^2 + C_S^2 + S_S^2) = \beta^2. \tag{3.21}$$

Similiar approach can be used for modeling thickness non-uniformity. In this case every parameter needs to be integrated over the distribution of thicknesses. For example

$$N_S = \int_{D_1}^{D_2} f(D)N(D)dD, \tag{3.22}$$

$$C_S = \int_{D_1}^{D_2} f(D)C(D)dD, \tag{3.23}$$

$$S_S = \int_{D_1}^{D_2} f(D)S(D)dD, \tag{3.24}$$

where D is the thickness, $f(D)$ is the distribution function of the thickness.

Treating depolarization caused by backside reflection is slightly different. Light passing through thick substrate can no longer be treated as coherent and it needs to be incoherently

added with light reflecting from the surface of substrate. This causes depolarization.

$$S_r = S_c + S_i = M_s S, \tag{3.25}$$

$$S_c = M_c S, \tag{3.26}$$

$$S_i = M_i S, \tag{3.27}$$

$$M_s = M_c + M_i, \tag{3.28}$$

where S_r is Stokes vector representing reflected light, S is Stokes vector representing incident light, S_c is Stokes vector representing light reflected from thin layer and S_i is Stokes vector representing light reflected from the back of the substrate. M_s is Mueller matrix of the whole sample and M_c and M_i are Mueller matrices of corresponding transformations. For example, let's consider an optical model made of one thin layer well within the coherent condition and thick transparent substrate satisfying incoherent condition.

Figure 3.3: Backside reflection model [13]

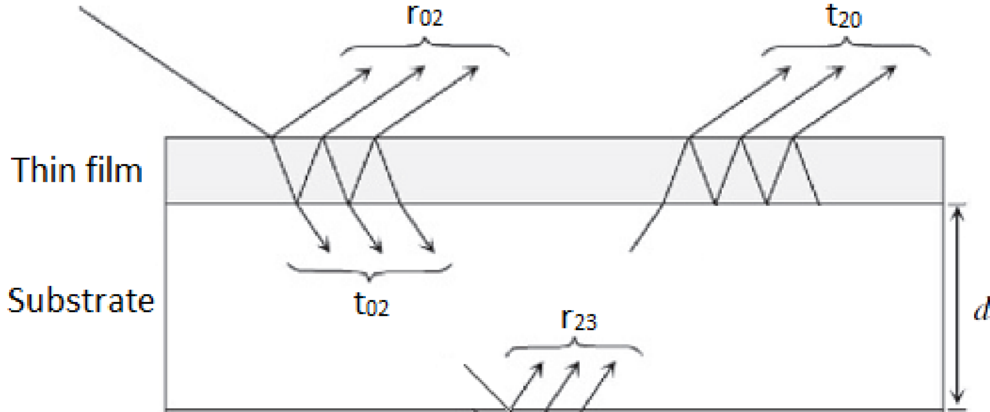

Reflection coefficient of the ray of light reflection from coherent thin layer will be

$$r^{02} = r^{01} + \frac{r^{12} t^{01} t^{01} \exp(-i2k_{z1} d)}{1 - r^{01} r^{10} \exp(-i2k_{z1} d)}, \tag{3.29}$$

where $k_z = \frac{2\pi}{\lambda} n_1 \cos\alpha$ and light is propagating in z direction. Coefficients r^{01}, r^{12} etc. are calculated using Fresnel equations. There will be different coefficients for p- and s-polarizations. Jones matrix of the ray reflecting from the surface thin layer is then

$$J_c = \begin{bmatrix} r_p^{02} & 0 \\ 0 & r_s^{02} \end{bmatrix}. \tag{3.30}$$

In the next step the Mueller-Jones matrix is calculated, as was discussed in the previous chapters.

The Jones matrix of second ray is given as

$$J_i = \begin{bmatrix} t_p^{02} & 0 \\ 0 & t_s^{02} \end{bmatrix} \begin{bmatrix} \exp(-ik_{z2}d) & 0 \\ 0 & \exp(-k_{z2}d) \end{bmatrix} \begin{bmatrix} r_p^{23} & 0 \\ 0 & r_s^{23} \end{bmatrix} \begin{bmatrix} \exp(-ik_{z2}d) & 0 \\ 0 & \exp(-k_{z2}d) \end{bmatrix} \begin{bmatrix} t_p^{20} & 0 \\ 0 & t_s^{20} \end{bmatrix}, \tag{3.31}$$

where $k_z = \dfrac{2\pi}{\lambda} n_2 \cos\alpha$ and

$$t^{02} = \frac{t^{01}t^{12}\exp(-ik_{z1}d)}{1 - r^{12}r^{01}\exp(-i2k_{z1}d)}, \tag{3.32}$$

$$t^{20} = \frac{t^{10}t^{21}\exp(-ik_{z1}d)}{1 - r^{21}r^{10}\exp(-i2k_{z1}d)}. \tag{3.33}$$

Again, Mueller-jones matrix is calculated and Mueller matrix describing the whole system is then obtained.

$$M_s = M_c + M_i \tag{3.34}$$

4. Au/Cr system on the glass substrate

The first sample analyzed in this thesis is Au/Cr multilayer on SF-10 glass substrate. It is a commercial sample fabricated by company Accurion for the purpose of a using it as a structure for the surface plasmon sensor. The structure according to the manufacturer is 44,8 nm thick gold layer and 2 nm thick chromium layer upon SF-10 glass substrate. The goal of my measurement is to test, whether assumed structure holds and to obtain the dielectric function of the gold layer. All data were measured using RC2 J.A. Woollam ellipsometer and analyzed using CompleteEase software.

4.1 Substrate analysis

Before measuring the actual sample, analysis of the substrate without films was conducted. The ellipsometry data were measured from both sides of the sample by colimated and focused beam and by transmission. Reflection data were measured at the incidence angles ranging from 40 to 80 degrees with 5 degree step. All measurements were done with 80 seconds acquisition time and the spectrum ranging from 0,729 to 6,425 eV. Afterwards the substrate was modeled by a simple substrate/roughness model. All data were fitted simultaneously and the dielectric funcion of the substrate was modeled by B-Spline (figure 4.4). The fit showed good agreement (figure 4.1 and 4.2) with measured data with the mean square error (MSE) 2,971.

Table 4.1: Comparison of calculated and tabulated [8] indices of refraction of SF-10 glass

E [eV]	Tabulated value	Calculated value
1,0096	1,6984	1,6979
3,0903	1,7776	1,7658

Figure 4.1: SF-10 side 1 fit

(a) NCS elements fit

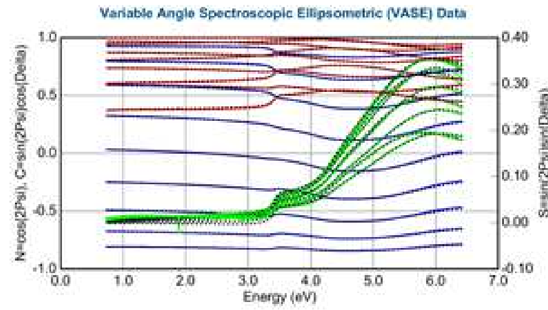

(b) Depolarization fit

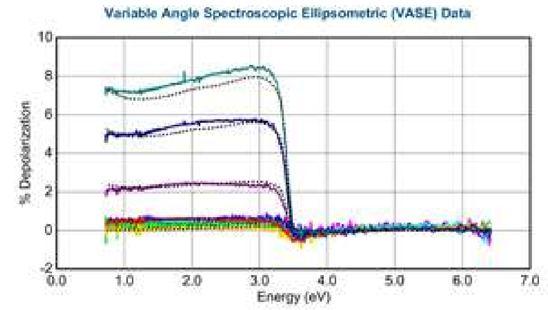

Figure 4.2: SF-10 side 2 fit

(a) NCS elements fit

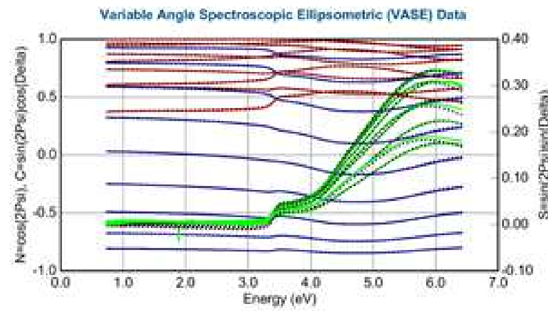

(b) Depolarization fit

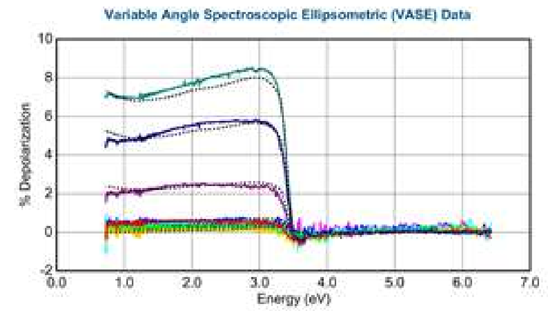

The model expected different roughness on both sides of the sample, 6,22 on one side and 4,44 on the other side. It is important to note that calculated roughness is only approximate and all we can say is, that there is thicker roughness on one side than on the other. This conclusion was then confirmed by AFM (atomic force microscopy, table 4.2).

Figure 4.3: SF-10 dielectric function

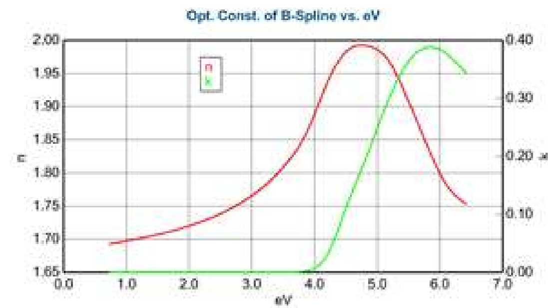

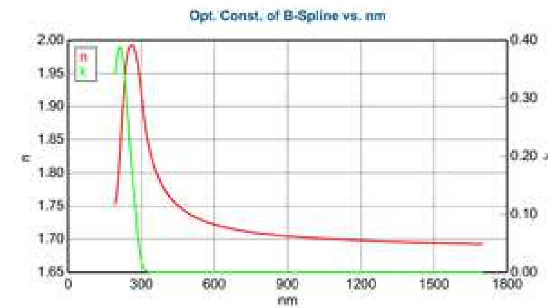

Table 4.2: AFM results

Sample	Roughness
SF-10 side 1	21,67 nm
SF-10 side 2	7,3 nm

4.2 Au/Cr system analysis

For the analysis of the actual sample the tabulated [9] dielectric functions of Au and Cr were used as initial values and the dielectric function of Au was then fitted to obtain more accurate data. The initial approach was to gain the data characterizing Cr and Au separately by using beams focused on the glass-Cr and the Au-air interfaces. However this approach proved to be less precise than simultaneously fitting the data from the transmission intensity, the front-side reflection and the glass-side reflection measurements (the ellipsometry data are measured by reflection off the sample through the subsrate and are not influenced by the surface layers). However, the data from the focused beam measurement were still used to validate model results. First the simple roughness/Au/Cr/Glass model was used. The Au dielectric function was fitted using B-spline model with tabulated [9] starting values. This model showed a good fit, however even better results (figure 4.5 - 4.7) were obtained by incorporating Intermix layers (EMA layer made of neighboring layers in 50/50 ratio) in Cr/glass and glass/air interfaces (figure 4.4). This result corresponds to the surface roughness of substrate, as the model calculated 5.12 nm on one side and 11,03 nm on the other side in agreement with results obtained by analyzing the substrate alone. All fitted parameters and their results can be seen in figure 4.4.

The dielectric function of gold was then also modeled using oscillator model (Drude + 2 Tauc-Lorentz oscilators). The resulting fits and dielectric funtions were compared (figure 4.8, table 4.3). The dielectric function of Cr (figure 4.9) was not fitted because of the lower sensitivity of model to its dielectric function. Fitting also Cr dielectric function would result in high correlation in the data.

Figure 4.4: Au/Cr/SF-10 multilayer model

Include Surface Roughness = ON Roughness = **1.95 nm** (fit)

Layer # 2 = Au_spline_param Thickness # 2 = **42.34 nm** (fit)
Layer # 1 = Cr Thickness # 1 = **1.75 nm** (fit)
Intermix Thickness = **5.12 nm** (fit)
Substrate = SF-10_spline_param Substrate Thickness = 1.0800 mm
Intermix Thickness = **11.03 nm** (fit)

Angle Offset = 0.000

- **MODEL Options**
  - Include Substrate Backside Correction = ON
    - Transmission SE Data = OFF Reverse Direction = OFF
    - # Back Reflections = 4.000 (MSA) % 1st Reflection = 100.00 (MSA)
  - Model Calculation = Ideal
  - **Multi Sample Analysis**
    - Add Fit Parameter Delete All Parms

Data Set	% 1st Reflection	Reverse Direction	Transmission SE Data	# Back Reflections
#1	100.00	OFF	OFF	4.000
#2	**89.17**	ON	OFF	**2.796**
#3	100.00	OFF	ON	4.000

Figure 4.5: Au/Cr/SF-10 multilayer front-side fit

(a) NCS elements fit

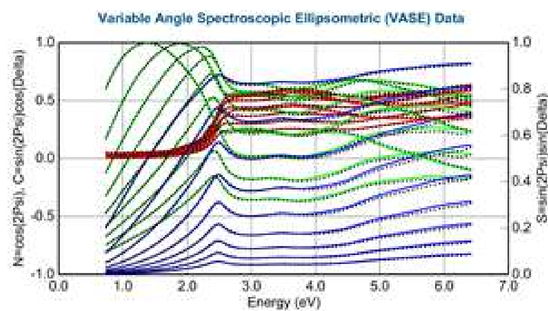

(b) Depolarization fit

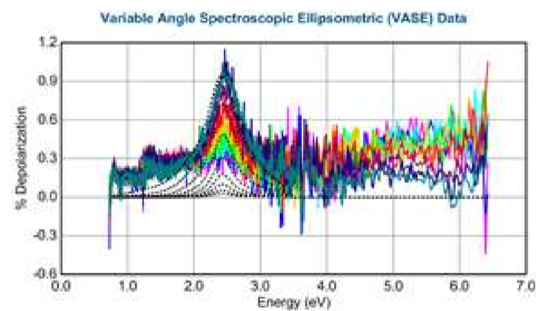

Figure 4.6: Au/Cr/SF-10 multilayer glass side fit

(a) NCS elements fit

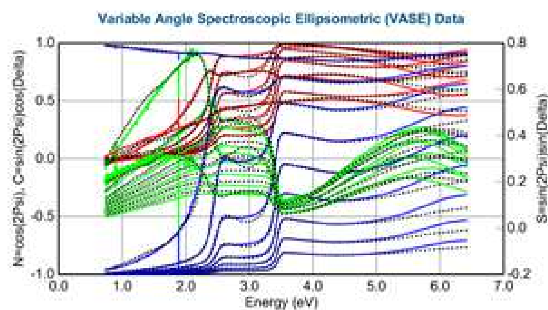

(b) Depolarization fit

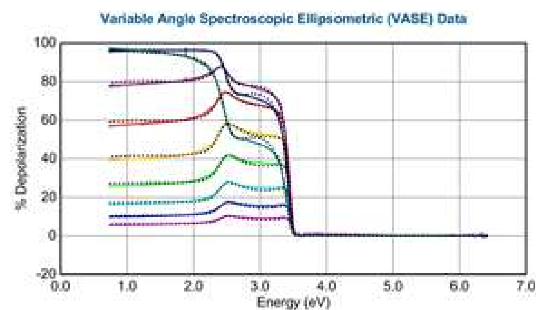

Figure 4.7: Au/Cr/SF-10 multilayer transmission intensity fit

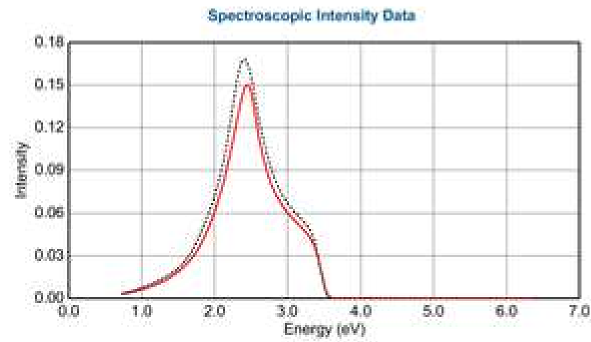

Figure 4.8: Au dielectric function comparison

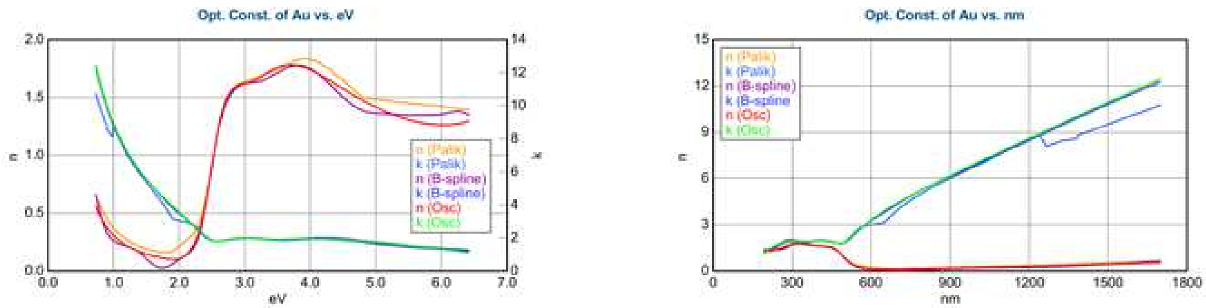

Figure 4.9: Cr dielectric function

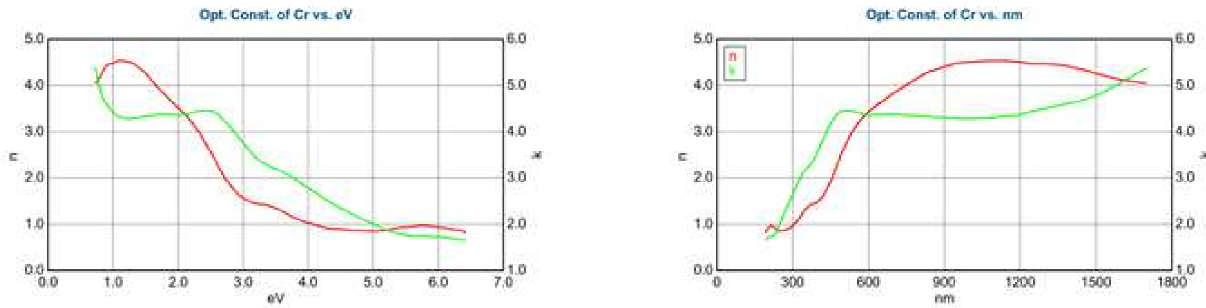

Table 4.3: Comparison of fits for different optical constants of gold

	Au (Palik) [9]	Au (B-spline)	Au (Osc)
MSE	22,753	13,774	13,779
Roughness	1 nm	1,95 nm	2,19 nm
Au thickness	46,82 nm	42,34 nm	42,31 nm
Cr thickness	1,48 nm	1,75 nm	1,75 nm

4.3 Conclusion

Obtained results agree with expectation. The system consists of 42,3 nm thick gold layer with 2 nm surface roughness (44,8 nm expected), 1,75 nm thick chromium layer (2 nm expected) and SF-10 glass substrate with different roughness on both sides. Different dielectric functions of Au are compared in the figure 4.8 and the fit results in the table 4.3. We concluded, that simultaneous fit of both-side Mueller-matrix ellipsometry together with normal incidence transmission data gives a good sensitivity to both upper and lower interface of the thin absorbing film on both side of the glass substrate.

5. Thin layers of Sn deposited on corning glass substrate

In this section the series of Sn layers deposited on corning glass substrate are analyzed, with the nominal thickness of 10, 20, 50 and 110 nm. The goal is to characterize a dielectric function of the Sn layers. All data were again measured using Mueller matrix ellipsometry from both sides of the sample and in transmission intensity mode. The same RC2 J.A. Woollam ellipsometer is used and data analyzed by the CompleteEase software. The reflection data were measured at the angle of incidence ranging from 45 to 70 degrees, with 5 degree step in the spectral range from 0,729 eV to 6,425 eV.

5.1 Substrate analysis

First, the substrate was characterized. We had at our disposal a sample of a substrate glass with its dielectric function already characterized by different laboratory. For the data analysis the simple roughness/substrate model was used. All data were fitted simultaneously using multi-data analysis feature of CompleteEase software with a simple roughness/substrate model. However, the data showed a slight variation between measured and generated values while using attached dielectric function. For better match with measured data, the corning glass dielectric function was fitted by a Tauc-Lorentz oscillator. The MSE improved from 6,591 to 1,139. It shows, that the attached dielectric function does not describe analyzed glass well. In figures 5.1 to 5.3 the data fits are shown and in figure 5.4 the calculated and attached dielectric functions of the subtrate are compared.

Figure 5.1: Corning glass front-side fit using fitted dielectric function

(a) NCS elements fit

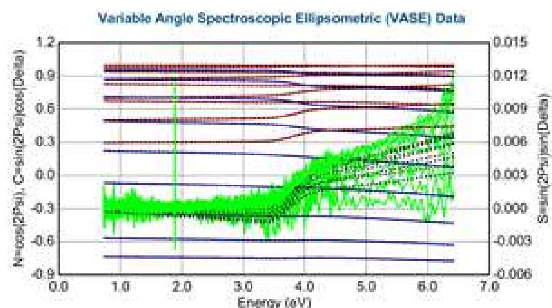

(b) Depolarization fit

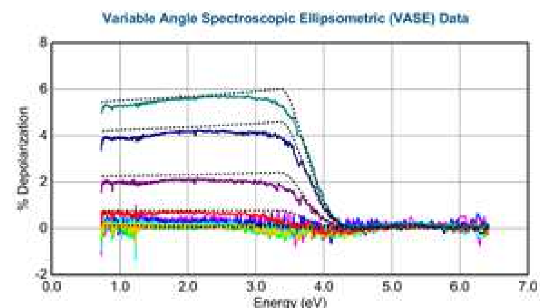

Figure 5.2: Corning glass back-side fit using fitted constants

(a) NCS elements fit

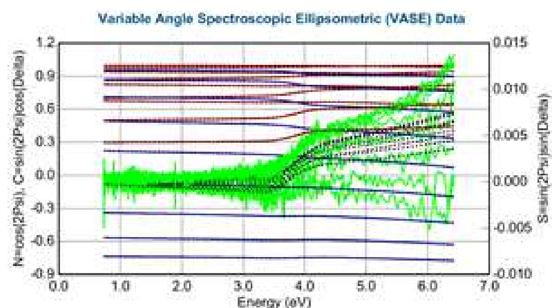

(b) Depolarization fit

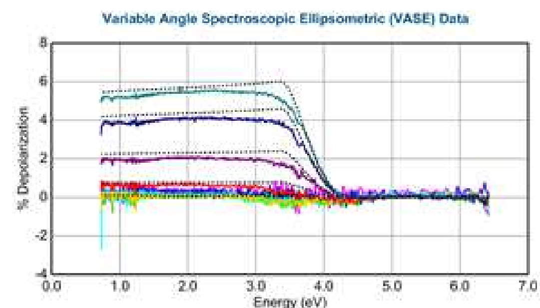

Figure 5.3: Corning glass transmission intensity fit using fitted dielectric function

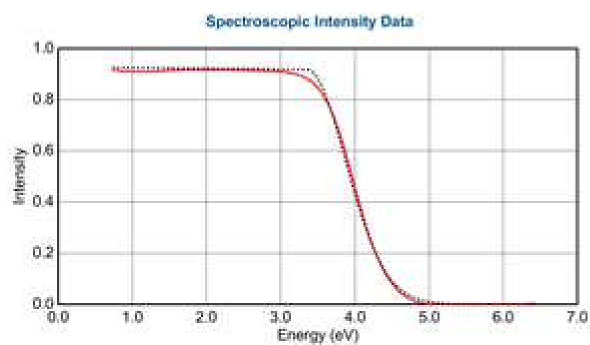

Figure 5.4: Attached and fitted dielectric function comparison

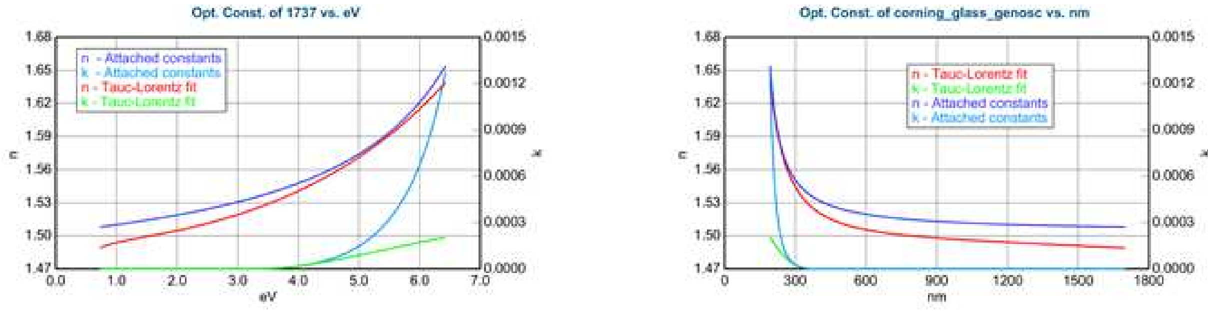

An interesting effect was observed during the data analysis (can also be observed at the S element of the Mueller matrix, figure 5.1a and figure 5.2a). The pseudo dielectric function of the sample varied for different angles of incidence at higher energies. This difference is slightly above measurement error and can be modeled by different roughness for every incident angle. It points to the presence of thin interface layer showing an anisotropic behaviour. This layer could originate from manufacturing process, where some dopant diffused into the glass or it could be a damaged layer created during polishing of the glass. However, this effect is very small and does not effect following measurements.

5.2 Sn - 110 nm

Next, the 110 nm thick Sn layer was analyzed. This sample is thick enough, for all the light to be absorbed, so the back and the front side of the sample has only one common parameter influencing its response, the Sn dielectric function. Furthermore, Sn layer thickness does not need to be fitted, as its value does not change the optical response of the system. However, the problem with this sample is a big surface roughness and surface oxidation. The AFM results showed 31 nm roughness (figure 5.5), which is beyond the correct applicability of EMA roughness approximation.

Many different models were tested, simple Sn/Roughness, Sn/SnO_2/Roughness, EMA consising of Sn/SnO_2 etc. The best fit was achieved while using a model incorporating intermix layer between Sn and SnO_2 layers and surface roughness on top (figure 5.6). The Sn optical constants were fitted using B-Spline model with tabulated initial values [9]. For the SnO_2 layer the dielectric function provided in CompleteEase software was used (figure 5.8b). Fitted parameters with their results can be seen in figure 5.6 and the resulting MSE was 7,955. The obtained dielectric function (figure 5.8a) is more realistic in energy region up to 4 eV, where the glass substrate starts to absorb and the light no longer reaches the Sn layer in the glass-side reflection

configuration (can be seen in figure 5.7b as the big shift in the data around 4 eV). However, even below this region the data are higly correlated as the thick oxidized roughness is at the limit of EMA models.

Figure 5.5: Sn - 110 nm AFM results

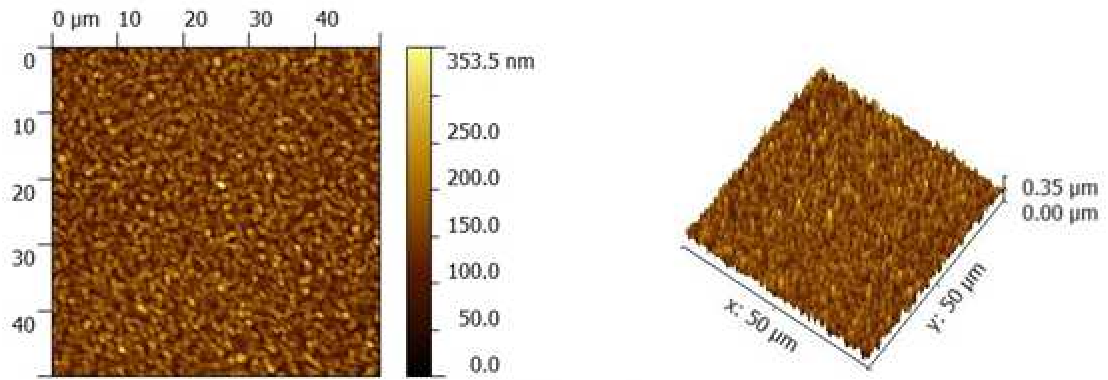

Figure 5.6: Sn - 110 nm multilayer model

Include Surface Roughness = ON Roughness = **18.85 nm** (fit)
+ Layer # 2 = SnO2 (Genosc) Thickness # 2 = **13.61 nm** (fit)
Intermix Thickness = **25.29 nm** (fit)
+ Layer # 1 = B-Spline Thickness # 1 = 104.94 nm
Intermix Thickness = **6.37 nm** (fit)
+ Substrate = corning_glass_genosc_upravene Substrate Thickness = 1.0000 mm
Intermix Thickness = 0.50 nm
Angle Offset = 0.000
- **MODEL Options**
Include Substrate Backside Correction = ON
Transmission SE Data = OFF Reverse Direction = OFF
Back Reflections = 5.000 % 1st Reflection = 100.00
Model Calculation = Ideal
- **Multi Sample Analysis**
Add Fit Parameter Delete All Parms

Data Set	Reverse Direction	Transmission SE Data
#1	OFF	OFF
#2	ON	OFF

While using substrate constants characterized in previous section the depolarization data (figure 5.9) showed variation between measured and generated data. These data are influenced only by two factors, the substrate dielectric function and its thickness. As the thickness would have to change by 0,5 mm to account for the data, the dielectric function of the glass has to vary from the previous measurement. By fitting the Tauc-Lorentz parameters a good match was achieved. This shows that provided glass has slightly different properties than the glass used for Sn layers deposition. Here obtained substrate‘s dielectric function was later used for all other Sn samples. Both dielectric functions are compared in figure 5.10.

Figure 5.7: Sn - 110 nm multilayer fit

(a) NCS elements front-side fit

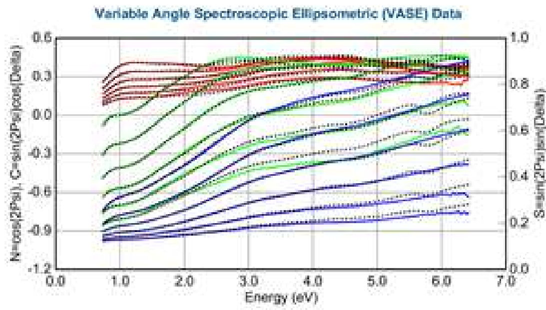

(b) NCS elements glass-side fit

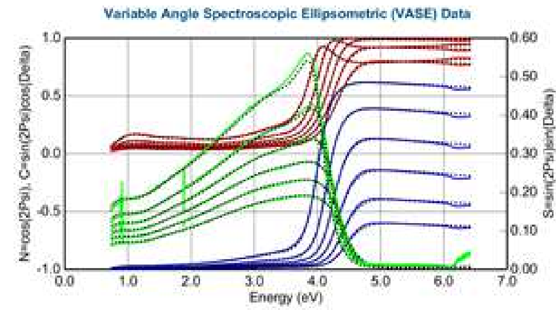

Figure 5.8: Sn and SnO_2 dielectric functions

(a) Sn fitted by B-spline

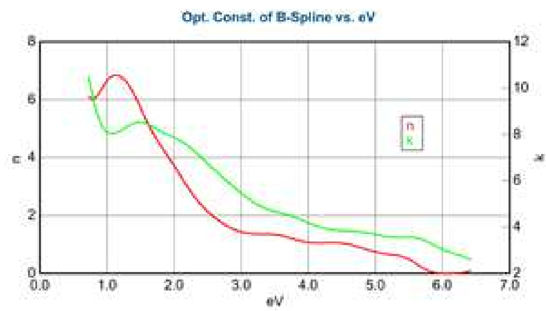

(b) SnO_2

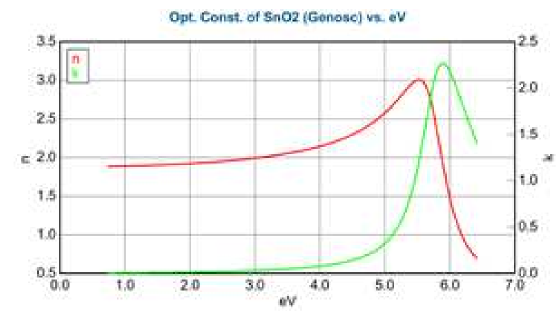

Figure 5.9: Sn - 110 nm multilayer glass-side depolarization fit

(a) Depolarization fit using the dielectric function of provided substrate

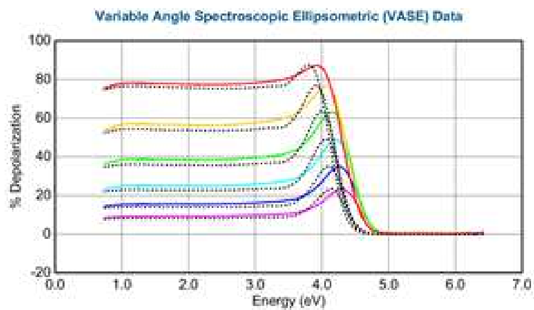

(b) Depolarization fit using fitted dielectric function

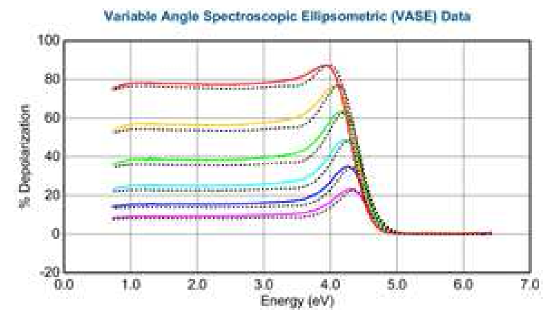

Figure 5.10: The dielectric function of provided substrate and fitted dielectric function comparison

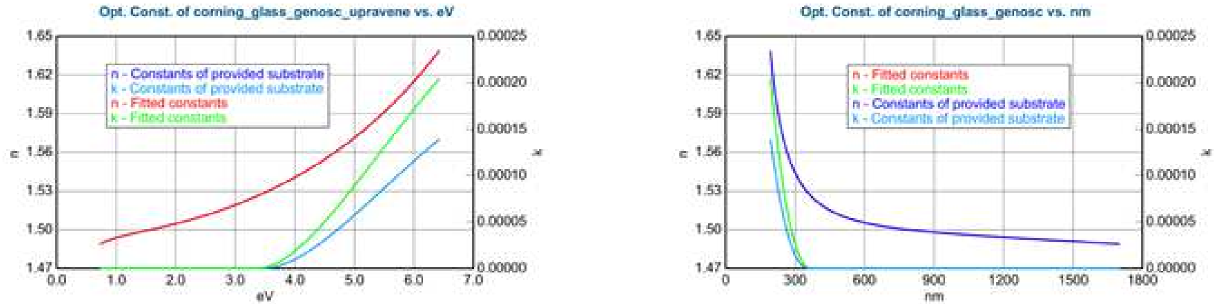

5.3 Sn - 50 nm

Again, many different models were tested as for 110 nm layers. The best fit was obtained for similiar model as was used for 110 nm layer (figure 5.11) and the same parameters were fitted. In this case, the light penetrated through the sample. The Sn thickness had to be added as a fitted parameter, what resulted in higher correlation between the fitted parameters. The same dielectric functions of SnO_2 layer and substrate are used. Intermix layer between Sn layer and substrate was fixed, due to high correlation with other data and its value was chosen by experience with different fits. The Sn dielectric function needed to be fitted again (figure 5.14b). Similiar trend was also observed with thinner layers and is discussed later. It appears that dielectric function of Sn changes with changing thickness of material. The model resulted in MSE 7,147 and fitted parameters with their results can be seen in figure 5.11.

Figure 5.11: Sn - 50 nm multilayer model

Include Surface Roughness = ON Roughness = **31.22 nm** (fit)
+ Layer # 2 = SnO2 (Genosc) Thickness # 2 = **1.20 nm** (fit)
Intermix Thickness = **13.49 nm** (fit)
+ Layer # 1 = B-Spline Thickness # 1 = **43.57 nm** (fit)
Intermix Thickness = 2.00 nm
+ Substrate = corning_glass_genosc_upravene Substrate Thickness = 1.0000 mm
Intermix Thickness = 0.50 nm
Angle Offset = 0.000
- **MODEL Options**
Include Substrate Backside Correction = ON
Transmission SE Data = OFF Reverse Direction = OFF
Back Reflections = 3.000 % 1st Reflection = 100.00
Model Calculation = Ideal
- **Multi Sample Analysis**
Add Fit Parameter Delete All Parms

Data Set	Reverse Direction	Transmission SE Data
#1	OFF	OFF
#2	ON	OFF
#3	OFF	ON

In figure 5.12a we can see that calculated data fits well for lower energies, but starts to diverge around 5 eV. This is the same effect observed at 110 nm thick layer and again shows smaller sensitivity of the model at region, where the substrate starts to absorb. Data from the front-side of the sample still did not show any depolarization (figure 5.12b). The data obtained from the glass-side of the sample showed a good fit (figure 5.13) The transmission data did not match the data well (figure 5.14a), however the transmitted intensity was very small and very sensitive to even small changes in the fitted parameters. The better fit could be obtained by weighted fit, but this resulted in substantial increase of MSE.

Figure 5.12: Sn - 50 nm multilayer front-side fit

(a) NCS elements fit

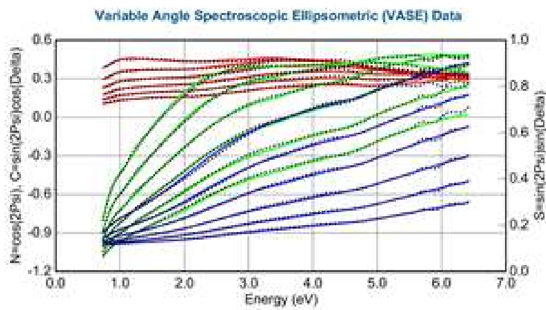

(b) Depolarization fit

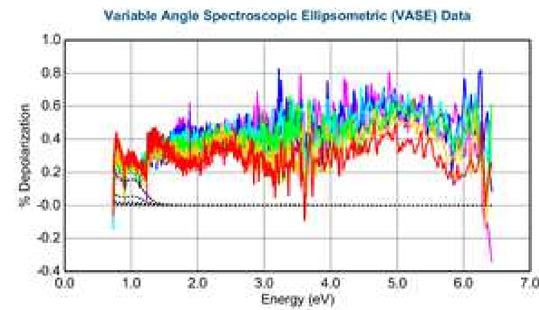

Figure 5.13: Sn - 50 nm multilayer glass side fit

(a) NCS elements fit

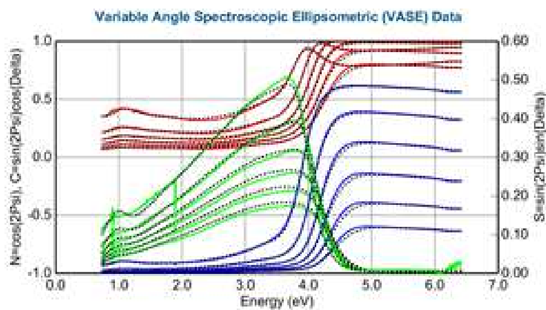

(b) Depolarization fit

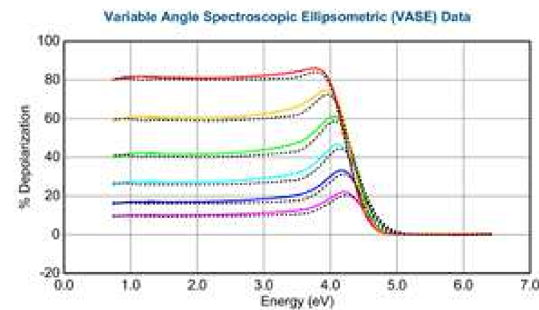

Figure 5.14: Sn - 50 nm transmission intensity fit and dielectric function

(a) Transmission intensity

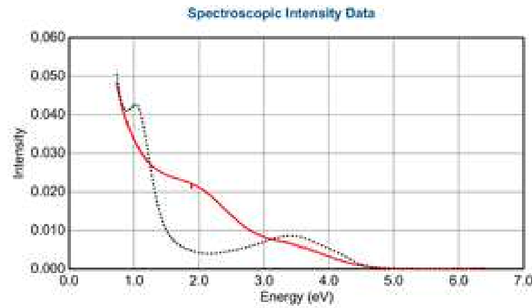

(b) Sn - 50 dielectric function

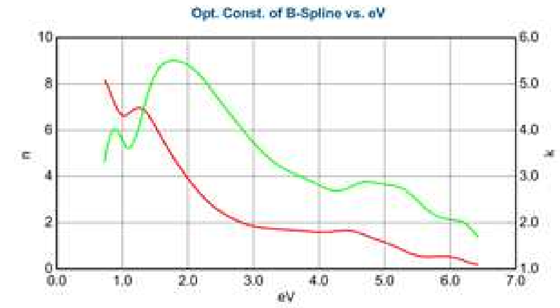

5.4 Sn - 20 nm

The same model (figure 5.15) and same fit parameters showed the best fit again. Fitted values can be seen in figure 5.15. MSE was 8,982. Sn thickness is now small enough to allow depolarization even from the front-side of the sample and the model fits relatively well with the measured data (figure 5.16b). In the case of 110 and 50 nm samples the glass-side reflection data were very similar, however now they start to change and they become sensitive even to oxidized surface layer (figure 5.17a). The Sn dielectric function had to be fitted again (figure 5.18). For this sample the transmission data were not measured and are not available for analysis.

Figure 5.15: Sn - 20 nm multilayer model

Include Surface Roughness = ON Roughness = 12.41 nm (fit)
Layer # 2 = SnO2 (Genosc) Thickness # 2 = 9.44 nm (fit)
Intermix Thickness = 9.11 nm (fit)
Layer # 1 = B-Spline Thickness # 1 = 26.39 nm (fit)
Intermix Thickness = 9.74 nm (fit)
Substrate = corning_glass_genosc_upravene Substrate Thickness = 1.0000 mm
Intermix Thickness = 0.50 nm
Angle Offset = 0.000
- MODEL Options
Include Substrate Backside Correction = ON
Transmission SE Data = OFF Reverse Direction = ON
Back Reflections = 3.000 % 1st Reflection = 100.00
Model Calculation = Ideal
- Multi Sample Analysis
Add Fit Parameter Delete All Parms

Data Set	Reverse Direction	Transmission SE Data
#1	OFF	OFF
#2	ON	OFF

Figure 5.16: Sn - 20 nm multilayer front-side fit

(a) NCS elements fit

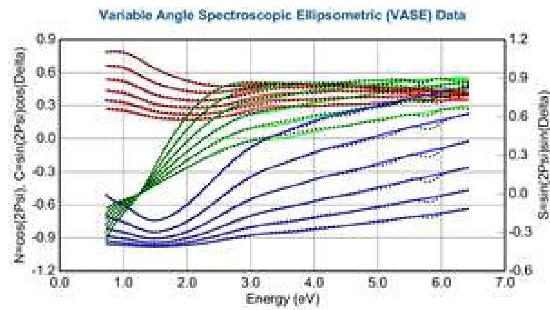

(b) Depolarization fit

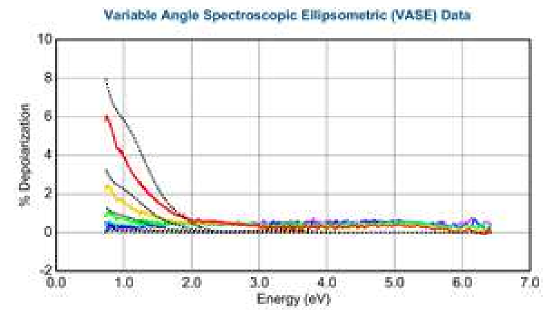

Figure 5.17: Sn - 20 nm multilayer glass side fit

(a) NCS elements fit

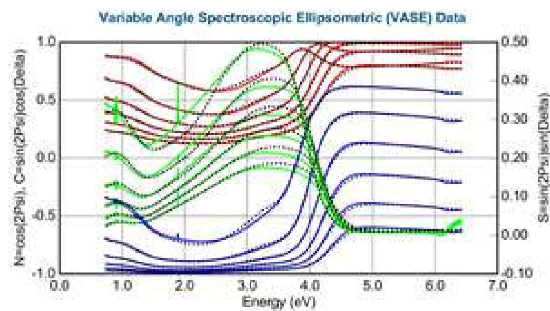

(b) Depolarization fit

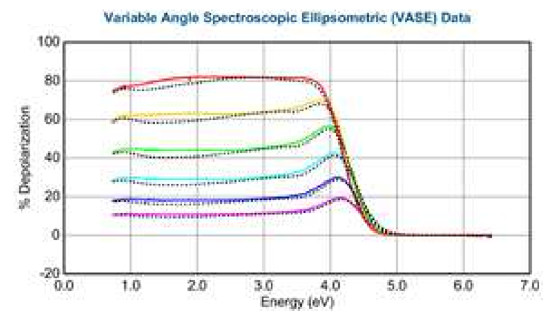

Figure 5.18: Sn - 20 dielectric function

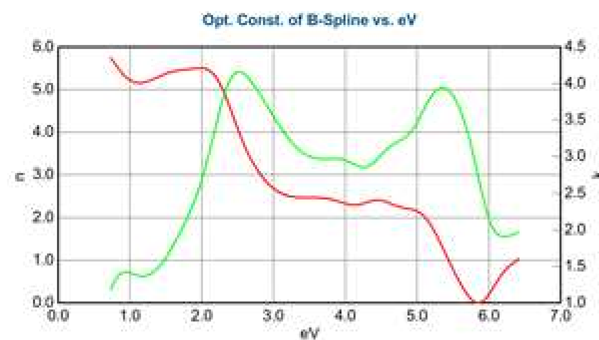

5.5 Sn - 10 nm

The same model (figure 5.19) showed the best fit again and its MSE was 8,227. The surface roughness fit showed 3,96 nm. It is thin enough, for an EMA model to be accurate. However, the fit showed 24,94 nm Sn thickness (figure 5.19), which varies substantially from the nominal value. Similiar trends in the data behaviour as were observed in the 20 nm thick sample continues and fits very well (figure 5.20 - 5.22) with the model. The depolarization from the front side of the

sample increased (figure 5.20b) and the glass-side data were even more sensitive to the surface layers (figure 5.21). Transmission data (figure 5.22a) fitted well. The Sn dielectric function changed again (figure 5.22b).

Figure 5.19: Sn - 10 nm multilayer model

Include Surface Roughness = ON Roughness = 3.96 nm (fit)
+ Layer # 2 = SnO2 (Genosc) Thickness # 2 = 3.41 nm (fit)
Intermix Thickness = 1.58 nm (fit)
+ Layer # 1 = B-Spline Thickness # 1 = 24.94 nm (fit)
Intermix Thickness = 5.46 nm (fit)
+ Substrate = corning_glass_genosc_upravene Substrate Thickness = 1.0000 mm
Intermix Thickness = 0.50 nm
Angle Offset = 0.000
- MODEL Options
Include Substrate Backside Correction = ON
Transmission SE Data = OFF Reverse Direction = OFF
Back Reflections = 4.000 % 1st Reflection = 100.00
Model Calculation = Ideal
- Multi Sample Analysis
Add Fit Parameter Delete All Parms

Data Set	Reverse Direction	Transmission SE Data
#1	OFF	OFF
#2	ON	OFF
#3	OFF	ON

Figure 5.20: Sn - 10 nm multilayer front-side fit

(a) NCS elements fit

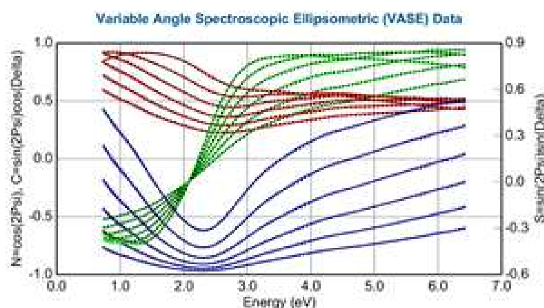

(b) Depolarization fit

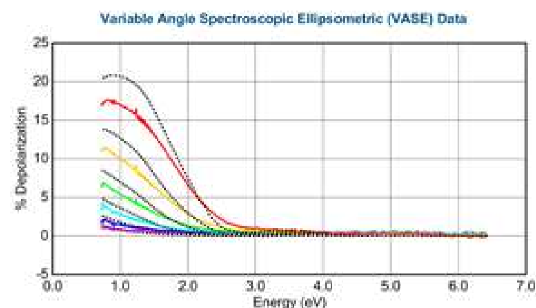

Figure 5.21: Sn - 10 nm multilayer glass side fit

(a) NCS elements fit

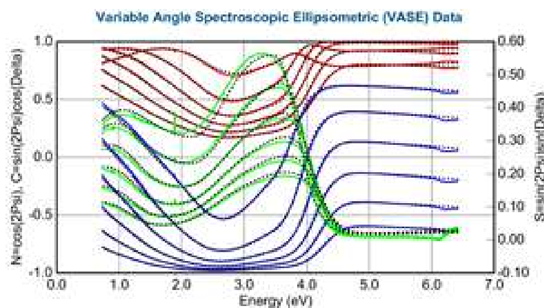

(b) Depolarization fit

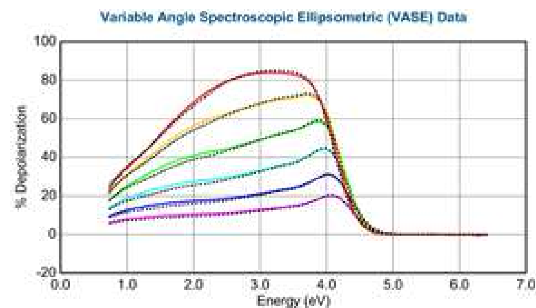

Figure 5.22: Sn - 10 nm transmission intensity fit and dielectric function

(a) Transmission intensity

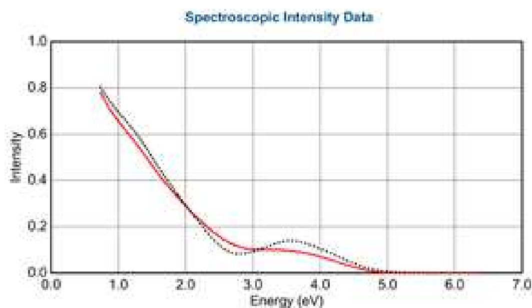

(b) Sn - 10 dielectric function

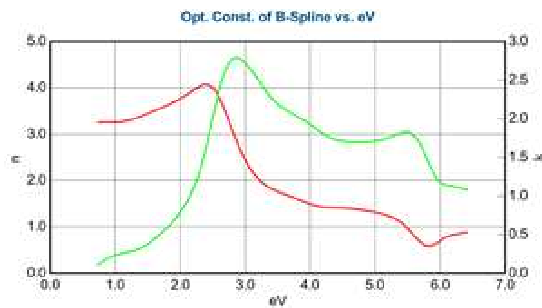

5.6 Discussion

The multilayer optical model used for the data analysis is not ideal representation of the oxidized surface roughness and high correlation between the data is present. However, the data fits relatively well, especially for energies up to 4 eV, where the substrate starts to absorb and the glass-side data are no longer sensitive to higher layers. The data shows a systematic change of Sn dielectric function as a function of the layer thickness (figure 5.23). This behaviour corresponds to the presence of different phases of Sn [17]. The dielectric function of 10 nm thick layer is characteristic by its interband transition around 2,4 eV corresponding to the semiconducting α-Sn, whereas the dielectric function of 110 nm sample is similar to the bulk β-Sn behaviour [9]. However, the transition between α and β phase is not clear. More complex models, incorporating different growth mechanisms by EMA and graded layers were tested, but no good fit was achieved. For further study, more samples, preferably stored in protective atmosphere to deny surface oxidation, would be needed.

Figure 5.23: Comparison of Sn dielectric functions

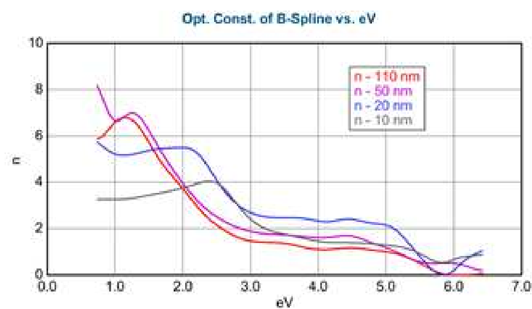

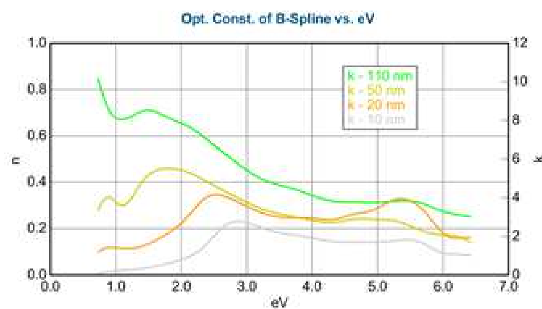

6. Anisotropic BBO crystal

BBO (low-temperature β phase of BaB_2O_4) is nonlinear optical crystal widely used in nonlinear optics. It has trigonal crystal structure and belongs to R3c space group. It is manufactured using top-seeded solution growth (TSSG) technique [19]. BBO crystals have a number of advantages for many applications in nonlinear optics. They have wide transparency optical region (189 - 3500 nm), broad phase-matching range, large nonlinear coefficients and high damage threshold [18]. Due to their optical properties BBO crystals are used for fourth and fifth harmonic generation of Nd-based laser systems, SHG of tunable Ti:sapphire lasers, optical parametric oscillators etc.

BBO crystals have negative unixial optical symmetry. It is described by sellmeier equation $(\lambda, \mu m)$ in the following way

$$n_0^2 = 2,7366122 + \frac{0,0185720}{\lambda^2 - 0,0178746} - 0,0143756\lambda^2 \quad (6.1)$$

$$n_e^2 = 2,3698703 + \frac{0,0128445}{\lambda^2 - 0,0153064} - 0,0029129\lambda^2 \quad (6.2)$$

Figure 6.1: BBO dielectric function

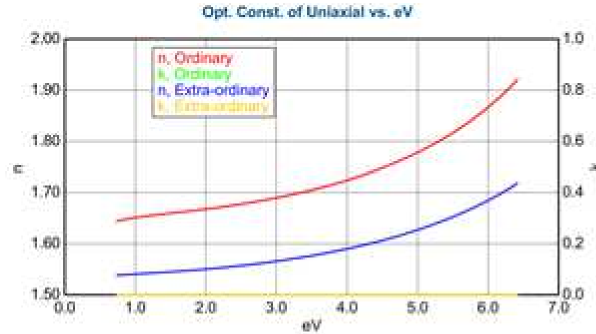

In this part of my thesis I calculated reflection coefficients of BBO/Air interface using Yeh's matrix method for special alignments of optical axis and then created a program using MATLAB software to calculate reflection coefficients for general rotation of the crystal.

6.1 Optical axis aligned with z-axis

The total matrix **M** of the interface will be given by

$$\boldsymbol{M} = [\boldsymbol{D_{Air}}]^{-1} \boldsymbol{D_{BBO}} \tag{6.3}$$

where

$$D_{Air} = \begin{pmatrix} 1 & 1 & 0 & 0 \\ n\cos\alpha & -n\cos\alpha & 0 & 0 \\ 0 & 0 & n\cos\alpha & n\cos\alpha \\ 0 & 0 & -n & n \end{pmatrix} \tag{6.4}$$

The crystal electric field in the crystal is described by following equaion.

$$\begin{pmatrix} \varepsilon_0 - N_y^2 - N_z^2 & 0 & 0 \\ 0 & \varepsilon_0 - N_z^2 & N_y N_z \\ 0 & N_y N_z & \varepsilon_e - N_y^2 \end{pmatrix} \begin{bmatrix} E_{0x} \\ E_{0y} \\ E_{0z} \end{bmatrix} = 0 \tag{6.5}$$

To calculate propagating eigenmodes

$$\det() = (\varepsilon_0 - N_y^2 - N_z^2)[(\varepsilon_0 - N_z^2)(\varepsilon_e - N_y^2) - N_y^2 N_z^2] = 0 \tag{6.6}$$

$$N_{z1,2} = \pm\sqrt{\varepsilon_0 - N_y^2} \tag{6.7}$$

$$N_{z3,4} = \pm\sqrt{\frac{\varepsilon_0(\varepsilon_e - N_y^2)}{\varepsilon_e}} \tag{6.8}$$

$$\boldsymbol{e_1} = \begin{bmatrix} 1 \\ 0 \\ 0 \end{bmatrix} \quad \boldsymbol{b_1} = \boldsymbol{N_1} \times \boldsymbol{e_1} = \begin{bmatrix} 0 \\ N_{z1} \\ -N_y \end{bmatrix} \tag{6.9}$$

$$\boldsymbol{e_2} = \begin{bmatrix} 1 \\ 0 \\ 0 \end{bmatrix} \quad \boldsymbol{b_2} = \boldsymbol{N_2} \times \boldsymbol{e_2} = \begin{bmatrix} 0 \\ -N_{z1} \\ -N_y \end{bmatrix} \tag{6.10}$$

$$\boldsymbol{e_3} = \begin{bmatrix} 0 \\ \varepsilon_e - N_y^2 \\ -N_y N_{z3} \end{bmatrix} \quad \boldsymbol{b_3} = \boldsymbol{N_3} \times \boldsymbol{e_3} = \begin{bmatrix} -\varepsilon_e N_{z3} \\ 0 \\ 0 \end{bmatrix} \tag{6.11}$$

$$
\boldsymbol{e_4} = \begin{bmatrix} 0 \\ \varepsilon_e - N_y^2 \\ N_y N_{z4} \end{bmatrix} \quad \boldsymbol{b_4} = \boldsymbol{N_4} \times \boldsymbol{e_4} = \begin{bmatrix} \varepsilon_e N_{z3} \\ 0 \\ 0 \end{bmatrix} \tag{6.12}
$$

With $\boldsymbol{e}$ and $\boldsymbol{b}$ vectors calculated the dynamic matrix of BBO crystal can be constructed.

$$
D_{BBO} = \begin{pmatrix} 1 & 1 & 0 & 0 \\ N_{z1} & -N_{z1} & 0 & 0 \\ 0 & 0 & \varepsilon_e - N_y^2 & \varepsilon_e - N_y^2 \\ 0 & 0 & -\varepsilon_e N_{z3} & \varepsilon_e N_{z3} \end{pmatrix} \tag{6.13}
$$

Now, the total matrix of the interface is known and by using (2.60 - 2.63) reflection coefficients can be calculated.

Figure 6.2: The calculated reflectivity of Air/BBO interface, optical axis aligned with z-axis

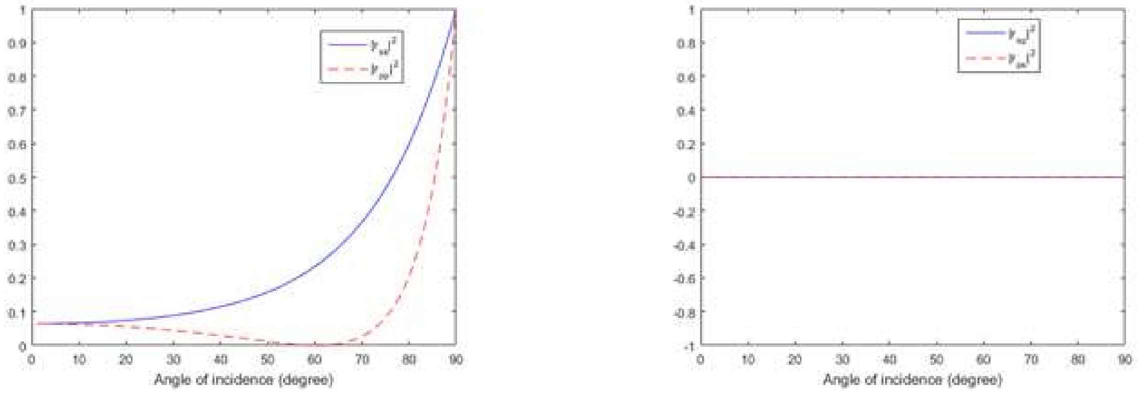

6.2 Optical axis aligned with y-axis

The same approach is used to calculate reflection coefficients of y-axis alignment. However, this time the homogenous equation is in form

$$
\begin{pmatrix} \varepsilon_0 - N_y^2 - N_z^2 & 0 & 0 \\ 0 & \varepsilon_e - N_z^2 & N_y N_z \\ 0 & N_y N_z & \varepsilon_0 - N_y^2 \end{pmatrix} \begin{bmatrix} E_{0x} \\ E_{0y} \\ E_{0z} \end{bmatrix} = 0 \tag{6.14}
$$

and

$$
N_{z1,2} = \pm\sqrt{\varepsilon_0 - N_y^2} \tag{6.15}
$$

$$
N_{z3,4} = \pm\sqrt{\frac{\varepsilon_e(\varepsilon_e - N_y^2)}{\varepsilon_0}}. \tag{6.16}
$$

Figure 6.3: The calculated reflectivity of Air/BBO interface, optical axis aligned with y-axis

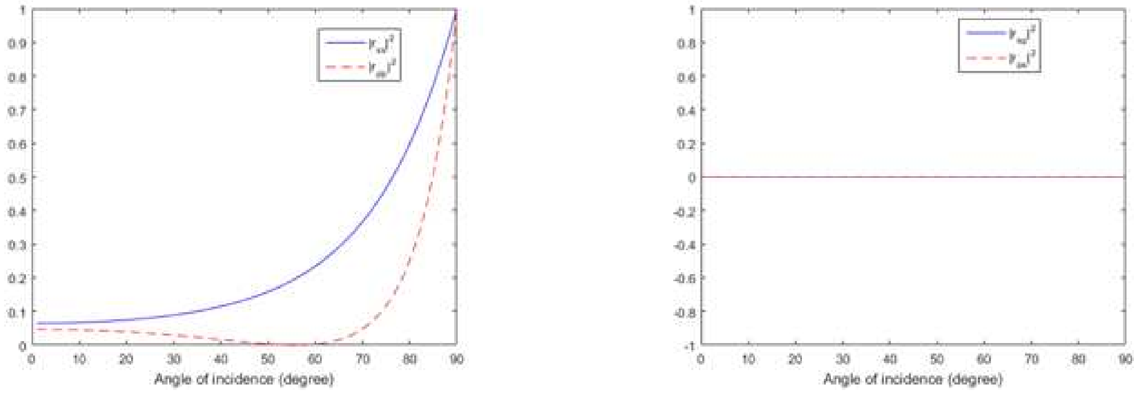

6.3 Optical axis aligned with x-axis

The same approach is used once again to calculate reflection coefficients of x-axis alignment. The homogenous equation takes form

$$\begin{pmatrix} \varepsilon_e - N_y^2 - N_z^2 & 0 & 0 \\ 0 & \varepsilon_0 - N_z^2 & N_y N_z \\ 0 & N_y N_z & \varepsilon_0 - N_y^2 \end{pmatrix} \begin{bmatrix} E_{0x} \\ E_{0y} \\ E_{0z} \end{bmatrix} = 0 \tag{6.17}$$

and

$$N_{z1,2} = \pm\sqrt{\varepsilon_e - N_y^2} \tag{6.18}$$

$$N_{z3,4} = \pm\sqrt{\varepsilon_0 - N_y^2}. \tag{6.19}$$

Figure 6.4: The calculated reflectivity of Air/BBO interface, optical axis aligned with x-axis

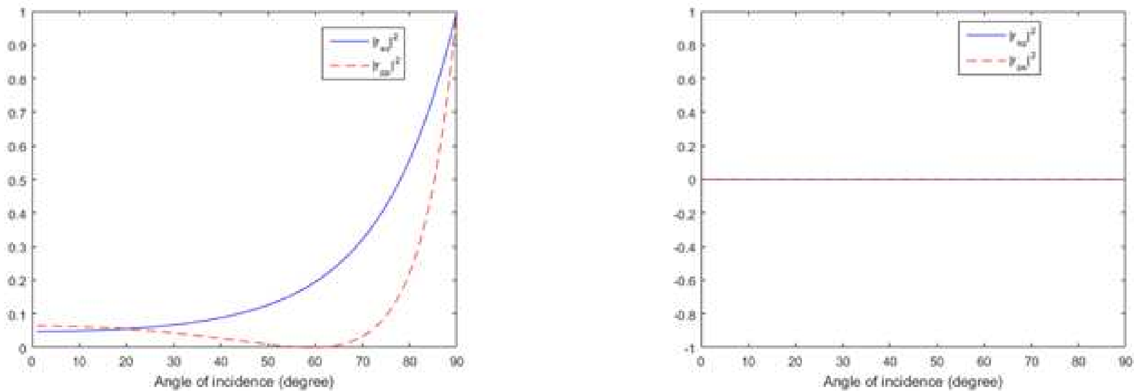

6.4 General alignment

We can see that in the case of alignments, where the optical axis is aligned with a coordinate axis, the r_{sp} and r_{ps} coefficients vanish, however eigenmodes experience different index of refraction every time. This fact is very useful during the data analysis. When the cross-polarization coefficients vanish, non-diagonal elements of Mueller matrix also vanish. This realization can be very helpful while determining the orientation of optical axis. At general orientation of the crystal, the cross-polarization coefficients do not vanish and their behaviour will influence ellipsometric response. Upon changing the angle of incidence coefficients also change and they will produce slight shift in the ellipsometric data. Upon rotating the sample the reflection coefficients also change, however they will show a periodical behaviour. Calculated coefficients then can be used to construct Jones and corresponding Mueller-Jones matrix.

Figure 6.5: The calculated reflectivity of Air/BBO interface, $\phi = 90°, \theta = 29°, \psi = 40°$

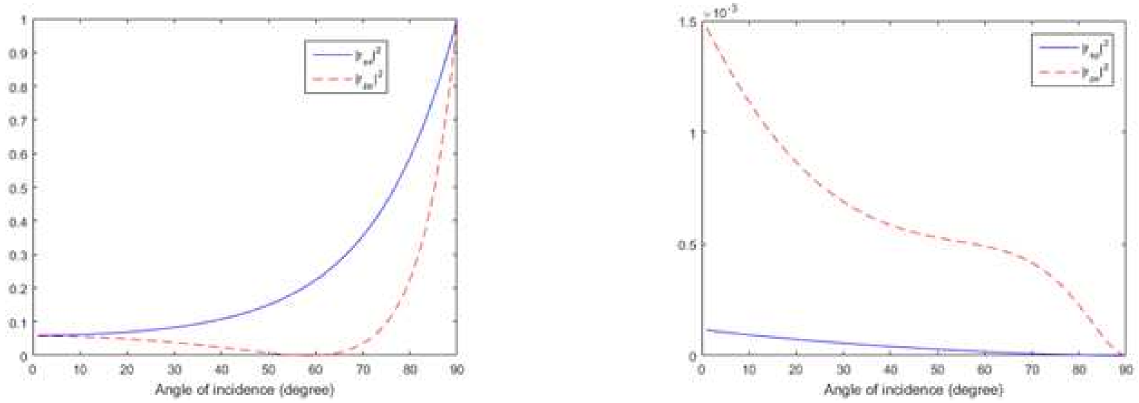

Figure 6.6: The calculated reflectivity of Air/BBO interface, $\phi = 90°, \theta = 29°, \psi =$ rotated, angle of incidence 40°

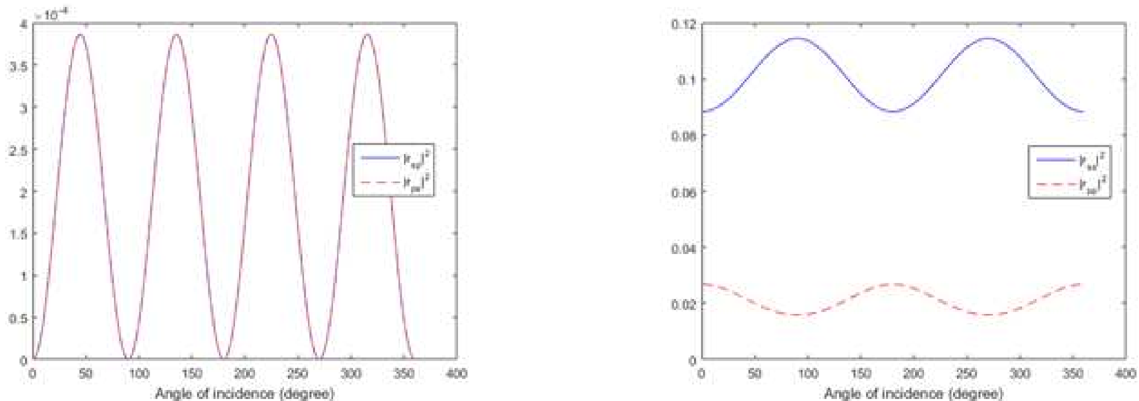

6.5 Measurement

The measurement was carried out on the BBO-605H sample [18]. It is 2 mm thick BBO crystal with $\theta = 29,2°$, $\phi = 90°$ orientation. Instead of the created MATLAB program, the CompleteEase software was used for the data analysis, due to the presence of more complex phenomena. First, the transmission was measured. In the figure 6.7, we can see dense interference in the data, typical for anisotropic materials, resulting from the phase difference of propagating eigenmodes and following polarization conversion at the second interface.

Figure 6.7: BBO Mueller matrix - transmission data,

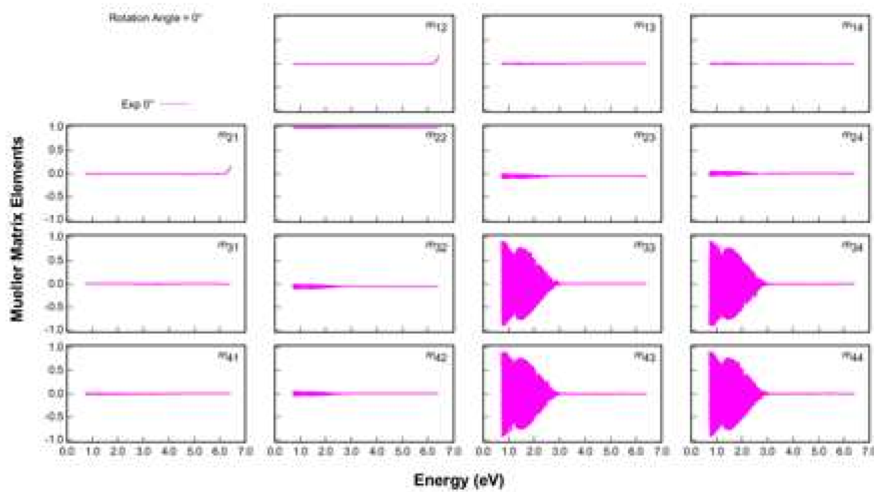

We can observe 2 phenomena. First, the amplitude of oscillations decreases with increasing energy. This is due to the finite bandwidth of the light detector and can be modeled in the CompleteEase software. Then there is a change in the trend of amplitude behaviour of the oscillations around 1,2 eV. This corresponds to the change of the CCD camera used during the measurement, which has different bandwith then camera used for higher energies. In the figure 6.8, both parts of the spectrum were modeled with different bandwidth parameters. We can see, that bandwidth 8 nm fits the data well up to 1,2 eV, where bandwidth 2 nm needs to be used. Only N,C and S elements of the Mueller matrix are shown for better illustration.

By modeling the frequency of oscillations, the thickness and orientation of the crystal was determined. The thickness was 2,1045 mm, $\phi = 88°$ and $\theta = 29,25°$ (catalog values: 2 mm, $\phi = 90°$ and $\theta = 29,20°$). The data fitted well as we can see in figure 6.9, however slight shift was observed when rotating the sample. This is caused by slight variations of the optical constants, as the oscillations are very sensitive to their value. This time the off-diagonal elements are chosen to demonstrate the effect.

Figure 6.8: BBO NCS elements - modeling of different bandwidth

(a) Bandwidth 8 nm

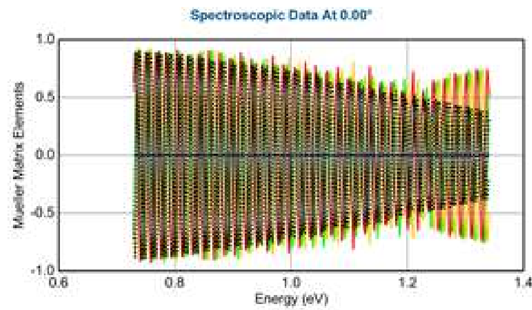

(b) Bandwidth 2 nm

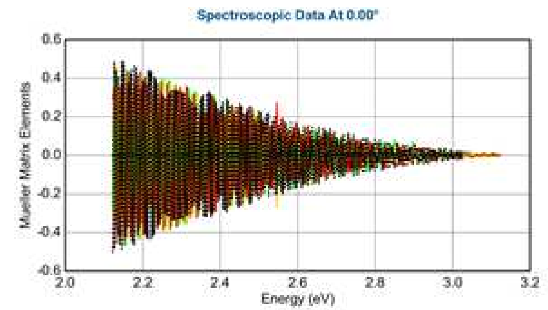

Figure 6.9: BBO off-diagonal elements - modeling the frequency of oscillations

(a) Rotation angle = 0°

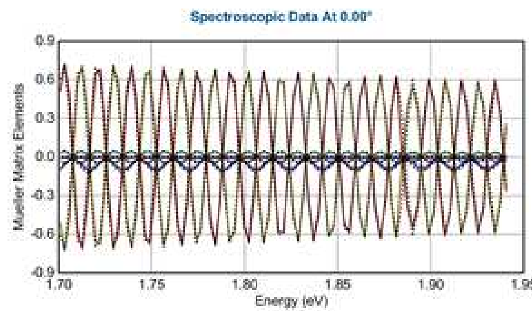

(b) Rotation angle = 95°

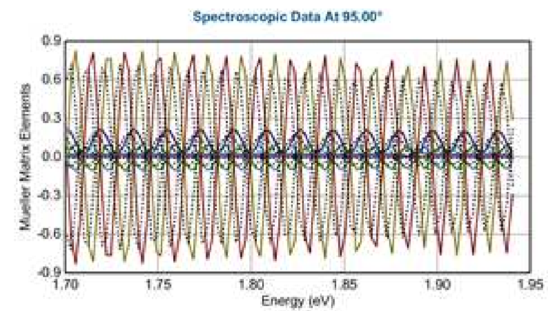

The last interesting effect observed is the deviation between the measured and calculated data for higher energies (around 6,25 eV). This deviation points to the begining of the absorbtion, which the used Sellmeier model is not able to describe (figure 6.10).

Figure 6.10: BBO NCS elements - deviation for higher energies

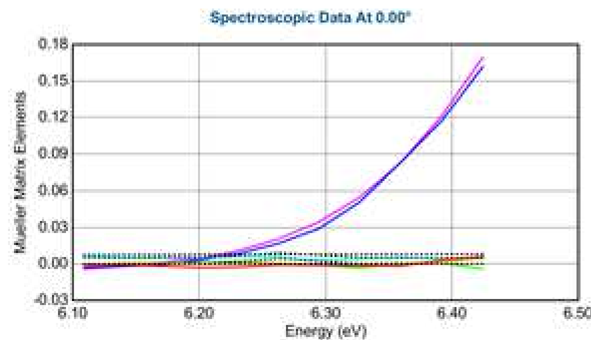

Next, the reflection data were measured. However, the precise behaviour of the sample was not possible to model, due to the presence of unknown coating. According to the catalog [18], there are 1 or 2 protective layers to prevent the absorbtion of H_2O by the BBO crystal, for mechanical protection and to act as anti-reflection coating. In the measured data (figure 6.11)

we can see 2 types of behaviour, the general shape of the curves and oscillations. The general shape is the result of light‘s interaction with the coating, however the oscillations are result of cross-polarization interactions during the backside reflection at the BBO crystal and could be modeled.

Figure 6.11: BBO chosen Mueller matrix elements - reflection data

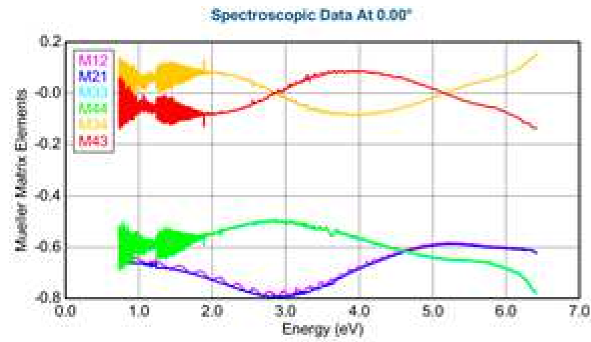

Without including finite bandwidth of the detector, the oscillations are very dense, as we can see in figure 6.12. The actual behaviour of the sample is then modeled by including finite bandwidth. The oscillations are becoming blurry for smaller energies. This effect is the same as the one observed in transmission data and depends on the bandwidth.

Figure 6.12: BBO M43 element - modeling the backside reflection

(a) Only backside reflection included

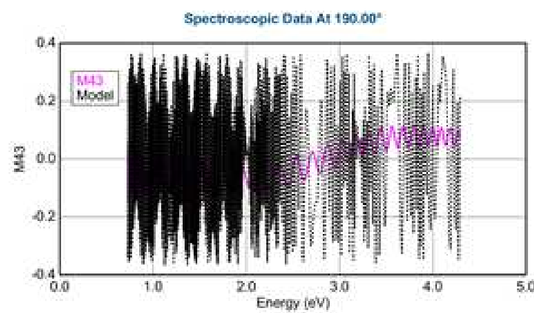

(b) Backside reflection + bandwidth 2,5 nm

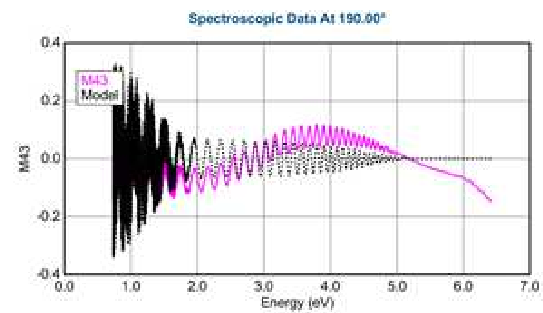

Another interesting behaviour was observed (figure 6.13). At rotation 0°, the top off-diagonal elements oscillates, while the bottom off-diagonal elements appears to vanish. At rotation 180° they switch, the top elements vanishes, while the bottom elements oscillates. This behaviour was modeled by the orientation of the crystal where $\phi = 88°$. The elements only appear to vanish, due to the inaccuracy of the measurement. This also confirms the observed orientation of the crystal during transmission measurement. It varies around 2° from the catalog value.

Figure 6.13: BBO Mueller matrix - vanishing of the off-diagonal elements

(a) Measured data

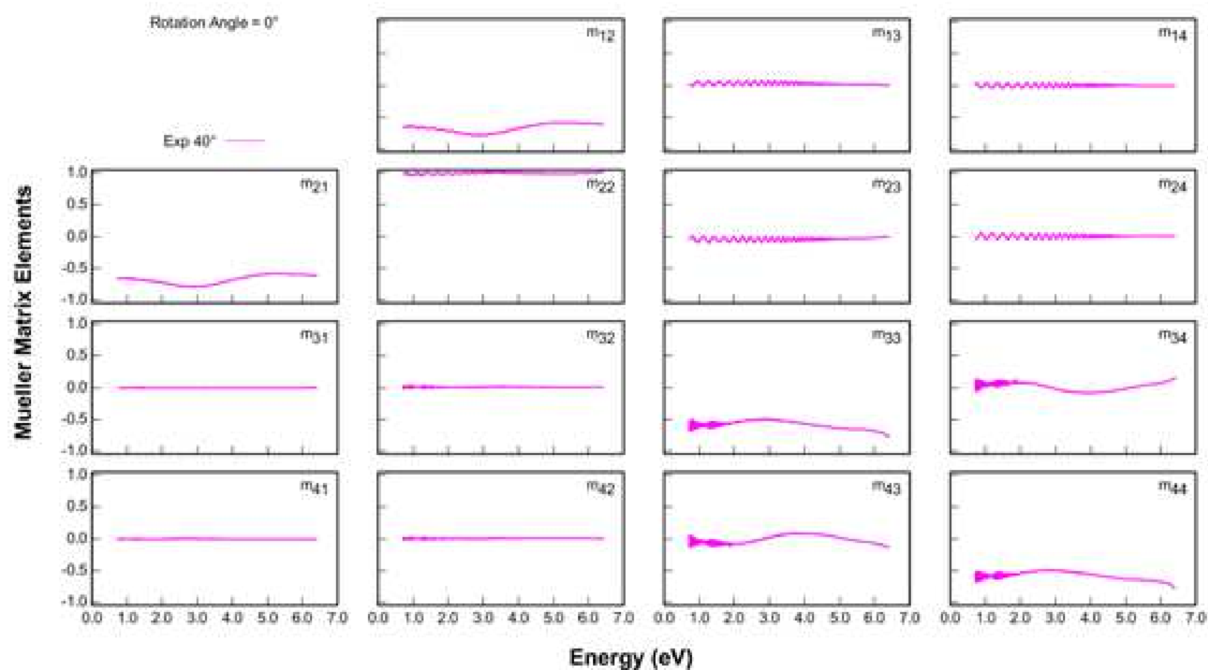

(b) Measured and generated data

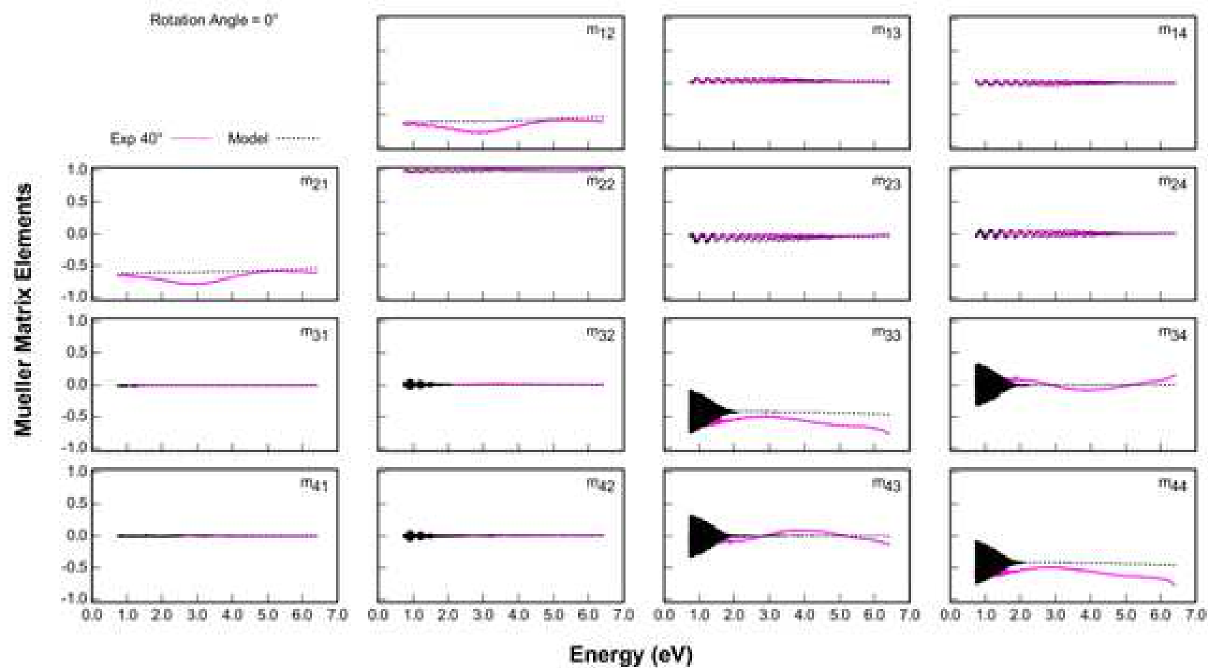

7. Conclusion

In this thesis the spectroscopic ellipsometry was used to characterize special samples. In the second chapter, the mathematical description of polarized light and its transformation by the sample was shown. Jones and Mueller calculus were presented. The behaviour of light in an anisotropic medium was described and the 4×4 matrix formalism was demonstrated as a method to calculate response of an anisotropic layered system. In the third chapter the Mueller matrix ellipsometry and general approach in data analysis were described. Different dielectric function models used during the data analysis were then presented and in the last section of the third chapter the depolarization modeling and its causes were discussed.

For the experimental part of this thesis, the Au/Cr/SF-10, Sn layers on glass substrate and anisotropic BBO crystal samples were measured with RC2 Woollam ellipsometer and analysed using CompleteEase software. For Au/Cr/SF-10 sample, the substrate was analyzed first using simultaneous fit of the front-side reflection, glass-side reflection and transmission intensity data. The analysis showed different surface roughness from both sides, this was confirmed by AFM. The same process was repeated for the actual sample. The Au dielectric function was fitted using different models and results were compared (figure 4.5, figure 4.9, table 4.3). The calculated structure agreed with expectations.

For the Sn layers, the substrate was again analyzed first. I had in my disposal dielectric function of the substrate analyzed by different laboratory, however the data did not fit the actual glass and the dielectric function was fitted to better match the data (figure 5.4). Furthermore, during the analysis of the actual samples, data showed, that glass used as substrate for deposition of Sn was slightly different from the one provided (figure 5.9 and 5.10) and was fitted again. Then the samples were analysed. Simultaneous fits of the front-side reflection, glass-side reflexion and transmission intensity were conducted for all samples. The model showed relatively good fit, even though the oxidized surface rougness was present. However, the Sn dielectric function changed with thickness (figure 5.23). This was due to the presence of α and β phases of Sn. The more complex models incorporating EMA composing of both phases or graded layers were tested,

however they did not match the measured data.

Last, the BBO crystal was analyzed. The reflection coefficients for different crystal orientations were calculated and the MATLAB program able to calculate sample‘s reflection in general orientation was created. However, for actual data analysis the CompleteEase software was used, due to the presents of backside reflection and more complex phenomena. The transmission of the sample was measured and then succesfully modeled (figure 6.8 - 6.10). Then the reflection data were measured and analyzed. There was a problem with an unknown protective coating influecing the shape of the measured data. Even though the precise behaviour of the sample was not possible to model, the typical effects caused by anisotropic BBO crystal were succesfully modeled (figure 6.12 - 6.13).

8. References

[1] KOSTER, G. a G. RIJNDERS (eds.). *In Situ Characterization of Thin Film Growth.* Woodhead Publishing, 2011. ISBN 978-1-84569-934-5.

[2] LI, Lingjie, Dongxia YAN, Jinglei LEI, Yuling HE, Jing XUA, Nianbing LIB a Shengtao ZHANGA. *Investigation Of Initial Stage Growth Of Anodic Zro2 Nanotubes By Spectroscopic Ellipsometry.* Electrochemistry Communications. 2014, (Volume 42), 13-16. DOI: doi:10.1016/j.elecom.2014.02.004.

[3] BEYENE, H. T., J. W. WEBER, M. A. VERHEIJEN, M. C. M. van de SANDEN a M. CREATORE. *Real time in situ spectroscopic ellipsometry of the growth and plasmonic properties of au nanoparticles on SiO2.* Nano Research. 2012-08, (Volume 5), 513-520. DOI: 10.1007/s12274-012-0236-z.

[4] GASPERA, Enrico Della, Stefano SCHUTZMANN, Massimo GUGLIELMI a Alessandro MARTUCCI. *Spectroscopic ellipsometry analyses of thin films in different environments: An innovative "reverse side" approach allowing multi angle measurements.* Optical Materials. 2011, (Volume 34), 79–84. DOI: doi:10.1016/j.optmat.2011.07.014.

[5] YAMAGUCHI, Shinji, Yoshio SUGIMOTO a Hiroyuki FUJIWARA. *Characterization of textured SnO2:F layers by ellipsometry using glass-side illumination.* Thin Solid Films. 2013, (Volume 534), 149–154. DOI: doi:10.1016/j.tsf.2013.02.018.

[6] YAMAGUCHI, Shinji, Yoshio SUGIMOTO a Hiroyuki FUJIWARA. *Ellipsometry analysis of a-Si:H solar cell structures with submicron-size textures using glass-side illumination.* Thin Solid Films. 2014, (Volume 565), 222–227. DOI: doi:10.1016/j.tsf.2014.06.025.

[7] MISRA, Soumyadeep, Wanghua CHEN, Martin FOLDYNA a Pere Roca i CABARROCAS. *A review on plasma-assisted VLS synthesis of silicon nanowires and radial junction solar cells.* Journal of Physics D Applied Physics. 2014, (47), 21. DOI: 10.1088/0022-3727/47/39/393001.

[8] RefractiveIndex.info *RefractiveIndex.info*. [online]9.4.2016 [cit. 2016-04-09].Dostupné z: http://refractiveindex.info/?shelf=glass& book=SF10& page=SCHOTT

[9] PALIK, Edward D. *Handbook of Optical Constants of Solids.*Orlando: Academic Press, 1998. ISBN 978-0-12-544415-6.

[10] [online]. [cit. 2016-05-15]. Dostupné z: http://4.bp.blogspot.com/-Q1rQHsPmJk4/TosORNTuTqI/AAAAAAAAFR0/sO4VP3EuV_s/s1600/reflections+4.png

[11] Inductiveload - Own work, Public Domain,. In: Wikipedia: the free encyclopedia [online]. San Francisco (CA): Wikimedia Foundation, 2001- [cit. 2016-05-15]. Dostupné z: https://commons.wikimedia.org/w/index.php?curid=4251521

[12] TOMPKINS, Harland a Eugene A IRENE. *Handbook of Ellipsometry (Materials Science and Process Technology).* William Andrew, 2006. ISBN 0815514999.

[13] FUJIWARA, Hiroyuki. *Spectroscopic Ellipsometry: Principles and Applications.* Wiley, 2007. ISBN 978-0-470-01608-4.

[14] AZZAM, R.M.A. a N.M. BASHARA. *Ellipsometry and Polarized Light.* 3rd reprint 1999. North Holland, 1988. ISBN 0444870164.

[15] YEH, Pochi. Optics of anisotropic layered media: A new 4 x 4 matrix algebra. *Surface Science.* 1980, 96.1–3, 41-53. DOI: 10.1016/0039-6028(80)90293-9.

[16] JOHS, Blaine a Jeffrey S. HALE. Dielectric function representation by B-splines. *Physica status solidi (a).* 2008, 205.4, 715-719. DOI: 10.1002/pssa.200777754.

[17] LÜTH, Hans. *Solid Surfaces, Interfaces and Thin Films.* Berlin: Springer Berlin Heidelberg, 2010. ISBN 978-3-642-13591-0.

[18] *Thin BBO Crystals for SHG* [online]. [cit. 2016-05-15]. Dostupné z: http://eksmaoptics.com/femtoline-components/femtoline-nonlinear-laser-crystals/thin-bbo-crystals-for-shg-of-ti-sapphire-laser-wavelength/

[19] CHUANGTIAN, Chen, et al. *Nonlinear Optical Borate Crystals: Principals and Applications:.* Wiley-VCH Verlag GmbH, 2012. ISBN 978-3-527-41009-5.